WAVEFIELD IMAGING USING THE ENERGY NORM

by

Daniel Carvalho Rocha Junior

© Copyright by Daniel Carvalho Rocha Junior, 2015

All Rights Reserved

A thesis submitted to the Faculty and the Board of Trustees of the Colorado School of Mines in partial fulfillment of the requirements for the degree of Master of Science (Geophysics).

Golden, Colorado

Date _____

Signed: _____
Daniel Carvalho Rocha Junior

Signed: _____
Dr. Paul C. Sava
Thesis Advisor

Golden, Colorado

Date _____

Signed: _____
Dr. Terrence K. Young
Professor and Head
Department of Geophysics

ABSTRACT

For various wavefield types, one can formulate a measurement of the mechanical energy that satisfies conservation laws. Based on this formulation, one can derive an *energy norm* that is applicable to wavefield imaging. Extending the concept of the norm to an inner product, one can compare two related wavefields. Therefore, an imaging condition can be defined as the inner product between the source and receiver wavefields at every spatial location. In this regard, the imaging condition based on the energy inner product accounts for wavefield directionality in space and time, overcoming some problems present in the conventional imaging condition.

I exploit the wavefield directionality information from the energy imaging condition to attenuate unwanted events in reverse time migrated (RTM) images. For acoustic wavefields, these unwanted events are characterized by the collinearity of the source and receiver ray-paths, and they are described as RTM backscattering artifacts. For elastic wavefields, these events are characterized by the fact that source and receiver displacement fields have the same polarization and wave propagation directions. In both acoustic and elastic cases, one can to attenuate these artifacts and produce high quality images.

Another application that uses the wavefield directionality is to enhance the full waveform inversion (FWI) gradient for acoustic wavefields. By enhancing wave events that are collinear and suppressing all other wave events, I am able to compute gradients that are more suitable for the inversion process.

Numerical experiments show the efficacy of these applications for synthetic models that emulate the complexity of subsurface structures found in exploration seismology, such as salt bodies, diffractors, dipping layers and faults.

TABLE OF CONTENTS

ABSTRACT iii

LIST OF FIGURES vii

LIST OF ABBREVIATIONS x

ACKNOWLEDGMENTS xi

DEDICATION xiii

CHAPTER 1 INTRODUCTION 1

CHAPTER 2 ACOUSTIC WAVEFIELD IMAGING USING THE ENERGY NORM . . 4

2.1 Introduction 5

2.2 Reverse-time migration 7

2.2.1 The L_2 norm and the conventional imaging condition 8

2.2.2 The energy norm and the proposed imaging condition 9

2.2.3 Wavefield orientation in the imaging condition 12

2.2.4 Backscattering attenuation 14

2.2.5 Amplitude and phase of the energy imaging condition 14

2.2.6 Examples 16

2.3 Full waveform inversion 17

2.3.1 Adjoint-state method 17

2.3.2 Application of the energy norm imaging condition to preserve the tomographic term 19

2.3.3 Examples 20

2.4 Conclusions . . . 21
2.5 Acknowledgments . . . 22
2.6 Appendix . . . 22
2.6.1 Relation with the Laplacian operator . . . 22
CHAPTER 3 ELASTIC WAVEFIELD IMAGING USING THE ENERGY NORM . . . 34
3.1 Introduction . . . 34
3.2 Theory . . . 37
3.2.1 Wavefield extrapolation . . . 37
3.2.2 Elastic wavefield energy . . . 37
3.2.3 Physical Interpretation . . . 40
3.2.4 Imaging condition . . . 40
3.2.5 Backscattering attenuation . . . 41
3.3 Examples . . . 44
3.4 Conclusions . . . 54
3.5 Acknowledgments . . . 54
3.6 Appendices . . . 54
3.6.1 Conservation of energy for an acoustic wavefield . . . 54
3.6.2 Frobenius product and norm . . . 56
3.6.3 Strain-energy function in isotropic media . . . 57
3.6.4 Terms not accountable for the total energy . . . 58
3.6.5 Elastic wave equation and continuity of second-order derivatives . . . 59
3.6.6 Christoffel equation for isotropic media . . . 60
CHAPTER 4 CONCLUSION . . . 62

REFERENCES CITED 64

LIST OF FIGURES

Figure 2.1 Schematic representation of (a) the source wavefield, (b) the receiver wavefield, and (c) conventional imaging, for a horizontal reflector at z=2.5 km in a 2-D experiment. The backscattered waves from source and receiver wavefields coexist in space and time and, consequently, overlap in the conventional image. 24

Figure 2.2 Schematic representation of the vector fields (a) $\Box U$, (b) $\Box V$, (c) the vector fields plotted together and (d) the imaging condition in equation 2.26. Notice that in (d), the backscattering events are characterized by orthogonal vectors $\Box U$ and $\Box V$, while the reflections are characterized by non-orthogonal vectors $\Box U$ and $\Box V$. 25

Figure 2.3 Experiment with a flat reflector, one source and one receiver on the surface at the locations $x = 2.5$ km and $x = 7.5$ km, respectively: (a) conventional imaging condition and (b) with Laplacian filter applied, and (c) energy norm imaging condition. 26

Figure 2.4 Same experiment geometry and model from Figure 2.3, but using the energy norm imaging condition to attenuate certain reflection angles: (a) normal-incidence reflections, (b) 15° reflections, (c) 30° reflections, and (d) 45° reflections. 26

Figure 2.5 Single-shot Sigsbee migrations. (a) and (b): sections of the stratigraphic velocity model overlaid by source and receiver positions (dark point and grey line at $x = 0$ km, respectively); (c) and (d): conventional images; (e) and (f) energy images. 27

Figure 2.6 Mutiple-shot Sigsbee migration: (a) stratigraphic velocity model, (b) conventional image, and (c) energy image. 28

Figure 2.8 Simple FWI experiments with an increase of 30% in velocity from the true model, without and with a free surface at $x = 0$ km, respectively: (a)/(b) Data residual, (c)/(d) conventional FWI gradient, (e)/(f) energy filtered FWI gradient, with the exponential filter applied on the image, and (g)/(h) on the wavefields. Most of the reflection artifacts are attenuated by the filtering. 30

Figure 2.9 Velocity models used in the Marmousi FWI experiment: (a) True velocity and (b) Initial velocity. 31

Figure 2.10 FWI gradients for a single shot at the first iteration: (a) conventional FWI gradient, (b) energy filtered FWI gradient, with the exponential filter applied on the image, and (c) on the wavefields. 32

Figure 2.11 FWI gradients for stacked shots at the first iteration: (a) conventional FWI gradient, (b) energy filtered FWI gradient, with the exponential filter applied on the image, and (c) on the wavefields. 33

Figure 3.1 Schematic plots showing the evolution of elastic plane-wave wavefields over time, originated by (a) a vertical source at $x = 0$ km and (b) a vertical receiver line at $x = 5$ km. Notice that (b) represents a wavefield propagating backwards in time. The thick arrows represent pure S-wave polarization, and the thin arrows represent the slowness vectors. 45

Figure 3.2 Schematic plots showing the evolution of elastic plane-wave wavefields over time, originated by (a) a vertical source at $x = 0$ km and (b) a vertical receiver line at $x = 5$ km. Notice that (b) represents a wavefield propagating backwards in time. The thick arrows represent pure P-wave polarization, and the thin arrows represent the slowness vectors. Note that the wavefields propagate faster than the ones in Figure 3.1 since P-wave velocity is faster than S-wave velocity. 46

Figure 3.3 Imaging conditions using displacement components for a horizontal reflector with a vertical displacement source at $x = 5$ km: (a) U_xV_x, (b) U_xV_z, (c) U_zV_x, and (d) U_zV_z image, where $\{U_x, U_z\}$ and $\{V_x, V_z\}$ are the horizontal and vertical components of the source and receiver wavefields, respectively. The type of artifacts that are present in all images occur due to the fake modes, which are generated when injecting an incomplete displacement field in the receiver wavefield. Polarity reversal at normal incidence occurs for (b) and (c). The reflector is present in the migration velocity to generate backscattering artifacts, which are visible in all images. 48

Figure 3.4 Imaging conditions using potentials for a horizontal reflector with a vertical displacement source at $x = 5$ km: (a) PP, (b) PS, (c) SP, and (d) SS image. Fake modes artifacts are also present in these images, analogously to Figure 3.3. The presence of a velocity contrast and the correlation between same wave modes in (a) and (d) generates backscattering artifacts, and the correlation between different wave modes in (b) and (c) generates polarity reversal at normal incidence. . . . 49

Figure 3.5 Individual terms of the energy imaging condition for a horizontal reflector present in the migration velocity, and a vertical displacement source at $x = 5$ km: (a) kinetic energy, (b) strain energy, (c) total energy and (d) imaging condition in equation 3.34. Comparing with other images from Figures 3.3-3.5, (d) is the only image with attenuated backscattering artifacts and without polarity reversal at normal incidence. 50

Figure 3.6 Images using conventional imaging conditions for a 3D elastic experiment with a horizontal reflector located at $z = 0.2$ km: (a) PS_y, (b) PS_z, (c) S_yP (d) S_zP, (e) S_yS_y, and (f) S_zS_z images. For images using correlation between the same wave modes, backscattering artifacts exist in (e) and (f); for the other images, which use correlation between different wave modes, polarity reversal occurs at normal incidence. 51

Figure 3.7 (a) PP image and images using energy imaging conditions for a 3D elastic experiment with a horizontal reflector located at $z = 0.2$ km, (b) total energy imaging condition, and (c) imaging condition from equation 3.34. Although (c) still has fake mode artifacts, stacking over shots attenuates this artifacts, as seen in (d), which is a stacked version of (c) using shots at every point at the surface. 52

Figure 3.8 Experiment on Marmousi model. (a) PP image, (b) Laplacian filter applied on the PP image in (a), (c) PS image, and (d) energy imaging condition in equation 3.34. The image in (d) shows no artifacts from polarity reversal and attenuated backscattering energy compared to the conventional images in (a) and (c), and higher quality compared to (b). . 53

LIST OF ABBREVIATIONS

Reverse Time Migration . . . . . RTM

Full Waveform Inversion . . . . . FWI

Center for Wave Phenomena . . . . . CWP

Conventional Imaging Condtion CIC

Gulf of Mexico . . . . . GoM

ACKNOWLEDGMENTS

In this thesis, I present a research project that was initiated by an interesting idea that came from the minds of my advisor, Paul Sava, and of Nicolay Tanushev, a fellow researcher at Z-Terra Inc. They represent the reason this project exists in the first place, and I dedicate my special thanks to them. In addition, they assisted me throughout this entire project, by giving me insights and knowledge for me to write a consistent theory section, and by conceiving helpful discussions on the numerical experiments shown here. Aside from this specific project, my advisor has assisted me in research and personal matters since the beginning of my graduate studies.

The faculty, staff and students from Center for Wave Phenomena (CWP), the research center of which I am part, helped me significantly in various ways. The members of the iTeam (group in CWP focused on wavefield imaging) gave me valuable insights from the many discussions that we had in our seminars, especially Esteban Diaz and Yuting Duan. Regarding administrative issues, Pam Kraus and Shingo Ishida have been always accessible and helpful during the time that I have been at CWP. My writing and communication skills have improved notably since my first days at CWP, thanks to Diane, the writing consultant in our research center. The other members in CWP faculty: Dave Hale (recently retired), Roel Snieder and Ilya Tsvankin, taught me relevant subjects that I incorporated in this thesis. A retired CWP faculty member, Ken Larner, has taught me valuable lessons for presenting to an audience effectively in his Professional Oral Communication course.

The consortium of companies which sponsors CWP funds my research and stipends. I am very grateful for the people who make this thesis research topic possible by funding. They also give relevant feedback in visits and in every CWP consortium meeting, which occurs yearly.

I would like to thank the members in my committee, Ilya Tsvankin, Paul Martin, Edwin Nissen and Michael Mooney, for them have found time in their busy schedules and accepted to be part of my committee. In addition, I would like to thank all the people involved in teaching me diverse topics in geophysics before and during my stay here at Colorado, especially my undergraduate advisor, Milton Porsani.

Finally, I would like to thank my family and friends for the personal support in my stay here in Colorado. These include my parents, Carol Rocha, Virginia Lacerda, Lorna Crawford, and many others.

For my parents, Daniel and Ivete.

CHAPTER 1

INTRODUCTION

Seismic wavefield imaging has become standard practice in the exploration industry, especially for oil and gas extraction purposes. The goal of this imaging methodology is to deliver accurate information about subsurface structures, so that resources such as oil and gas can be correctly mapped. Various types of algorithms that implement wavefield imaging are available in industry and academia, and the one that best handles complex geological settings, as those found in the Gulf of Mexico (GoM), is Reverse Time Migration (RTM) (Baysal et al., 1983; McMechan, 1983; Whitmore, 1983).

Although RTM is considered the best available wavefield imaging algorithm for complex structures, a problem that hampers its output arises from the presence of sharp changes in the velocity model used for imaging. Commonly, these sharp constrasts occur at boundaries of salt bodies, and these interfaces create backscattered reflections for both source and receiver wavefields during the wavefield extrapolation process. This problem manifests in the image as low wavenumber events, known as RTM backscattering artifacts, which mask reflectors in most parts of the image. These artifacts appear in acoustic images (Guitton et al., 2007; Yoon and Marfurt, 2006; Youn and Zhou, 2001) and in elastic images, especially when one correlates the same wave modes between the source and receiver sides (Chen and Huang, 2014; Denli and Huang, 2008).

Even though the backscattered events are harmful to the imaging process, these events, together with diving and direct waves, are of interest in wavefield tomography methods (Diaz and Sava, 2015). In wavefield tomography, the gradient of the objective function contains the tomographic term, which has useful information about the velocity model, and the migration term, i.e., the reflections or cross-talk events. The migration term adds nonlinearity to the tomographic objective function, leading to slow convergence towards the

true model. Enhancing the tomographic term of the gradient relative to the migration term could mitigate this problem, expediting the convergence towards the true velocity model (Shan et al., 2014; Tang et al., 2013).

This thesis shows different approaches for addressing these problems, all based on the same idea: the use of energy-norm based imaging conditions that exploit wavefield directionality. By using this directionality information, an imaging condition can distinguish useful events from unwanted events in the comparison between source and receiver wavefields. The energy norm is quite general, and it can be defined for any type of wavefield (acoustic, elastic, etc). Therefore, I treat similar problems for different wavefield types in each one of the chapters of this thesis.

In the second chapter, I introduce the definition of the energy norm, which is derived using conservation laws and a specific wave equation (in this case, constant density acoustic). The imaging condition based on this norm can be written in terms of energy vectors, which describe the wavefield directionality through space-time. In order to suppress unwanted events, such as RTM backscattering, I use the energy imaging condition in such a way that the unwanted energy vectors for source and receiver wavefields become orthogonal, leading to reduced contribution from their energy inner product in the image. In addition, a combination of two different imaging conditions based on the energy norm to attenuate different reflection angles leads to a filtering procedure to minimize the migration term in full waveform inversion (FWI) gradients.

In the third chapter, I present the energy norm for elastic isotropic wavefields and how it can be applied to wavefield imaging, leading to improved results for elastic RTM. Similarly to the acoustic case, when sharp interfaces are present in the velocity model, conventional elastic images fail to deliver a good image due to backscattering artifacts, which are characterized by events that have the same polarization and propagation direction. Another problem in elastic RTM arises when imaging with different wave modes from the source and receiver wavefields, i.e., polarity reversal at normal incidence (Balch and Erdermir, 1994; Duan and

Sava, 2014a; Yan and Sava, 2008). In contrast, the images obtained by the energy norm are of high quality and accurately show the subsurface structures, even when the velocity model has sharp interfaces and the correlated wavefields contain converted waves.

CHAPTER 2

ACOUSTIC WAVEFIELD IMAGING USING THE ENERGY NORM

Submitted to Geophysics for publication

Daniel Rocha[*,1], Nicolay Tanushev[2] and Paul Sava[1]

Wavefield energy can be measured by the so-called *energy norm*. We extend the concept of norm to obtain the energy inner-product between two related wavefields. Considering an imaging condition as an inner product between source and receiver wavefields at each spatial location, we propose a new imaging condition that represents the total reflection energy. Investigating this imaging condition further, we find that it accounts for wavefield directionality in space-time. Based on the directionality discrimination provided by this imaging condition, we apply it to attenuate backscattering artifacts in reverse-time migration (RTM). This imaging condition can be designed not only to attenuate backscattering artifacts, but also to attenuate any selected reflection angle. By exploiting the flexibility of this imaging condition for attenuating certain angles, we develop a procedure to preserve the type of events that propagate along the same path, i.e., backscattered, diving and head waves, leading to a suitable application for full waveform inversion (FWI). This application involves filtering the FWI gradient to preserve the tomographic term (waves propagating in the same path) and attenuate the migration term (reflections) of the gradient. We illustrate the energy imaging condition applications for RTM and FWI using numerical experiments in simple (horizontal reflector) and complex models (Sigsbee and Marmousi).

* Corresponding author. Direct correspondence to drocha@mines.edu
[1] Center for Wave Phenomena, Colorado School of Mines, 924 16th St., Golden, CO 80401
[2] Z-Terra Inc., 17171 Park Row Dr. #247, Houston, TX 77084

2.1 Introduction

Wavefield extrapolation is commonly known as a mathematical technique for numerically generating a wavefield in space and time, using a known portion of the wavefield itself (Margrave and Ferguson, 1999). One can use wavefield extrapolation to form an image of the subsurface, which is related to the Earth's reflectivity, in the case where the velocity is known and sufficiently accurate or to obtain subsurface velocity information by solving an inverse problem. In particular, when the two-way wave-equation is used, the former method is called reverse-time migration (Baysal et al., 1983; Levin, 1984; McMechan, 1983), and the latter is called full waveform inversion (Gauthier et al., 1986; Lailly, 1983; Plessix et al., 2013; Tarantola, 1984).

Reverse-time migration (RTM), as well as other wave-equation imaging procedures, obtains an image of a reflector in the subsurface in two steps. The first step is to extrapolate two wavefields from surface seismic data, one originating at the source location and the other at receiver locations. The second step is to crosscorrelate these extrapolated wavefields in time and form an image as the zero-lag correlation (Clærbout, 1985). This procedure is based on the assumption that, for the single scattering approximation, the reflector is at the location where source and receiver wavefields coexist in time and space (Cohen and Bleistein, 1979; Oristaglio, 1989; Perrone and Sava, 2014). At the source location, the real injected pressure function is often unknown and an estimated source function is used, i.e., the source wavefield is synthetic for the majority of RTM implementations.

Full waveform inversion (FWI) using two-way wave-equation obtains a velocity update by crosscorrelation between the state wavefield, which is similar to the source wavefield in RTM, and the adjoint wavefield (Hindlet and Kolb, 1988; Plessix, 2006; Tarantola, 1984). The adjoint wavefield is extrapolated from a data residual, which is often defined as the difference between observed and synthetic data. The velocity model is updated by minimizing the residual in a least-square sense. Mathematically, this velocity update is associated with the gradient of an objective function, which represents a norm of the residual vector.

Both RTM and FWI methods rely on the crosscorrelation of wavefields, which causes some problems. On one hand, besides imaging reflectors, RTM also outputs spurious artifacts caused by the crosscorrelation of wavefields propagating in the same direction: backscattering, head and diving waves (Diaz and Sava, 2015). For FWI, on the other hand, the crosscorrelation of wavefields propagating in the same direction forms low-wavenumber events that translate into useful velocity update information (tomographic term); and the imaged reflectors (migration term) represent the source of non-linearity that prevents the optimization from converging (Mora, 1989). Given these problems, alternatives to crosscorrelation have been investigated for both RTM and FWI (Chang and McMechan, 1986; Fletcher et al., 2005; Gao et al., 2012).

For RTM, the simplest and most common approach for overcoming the low-wavenumber events is to apply a high-pass filter. The Laplacian filter serves this purpose (Youn and Zhou, 2001) and is also convenient regarding processing cost since it involves post-imaging filtering. Other post-imaging filtering techniques are shown in the literature (Guitton et al., 2007; Xu et al., 2014), but such techniques do not account for multipathing. This filtering can also be applied prior to imaging by using the propagation directions of wavefields obtained by Poynting vectors (Costa et al., 2009; Yoon and Marfurt, 2006) or by wavefield decomposition (Liu et al., 2011; Suh and Cai, 2009) to attenuate wavefields traveling in the same direction. However, the imaging condition using Poynting vectors requires the design of a weighting function; and wavefield decomposition only separates wavefields into their up-going and down-going parts, resulting in unaltered backscattering artifacts from nearly horizontal reflected waves.

For FWI, in order to preserve the tomographic component and attenuate the migration component in the velocity update, some authors have used filtering on the FWI gradient (Albertin et al., 2013; Alkhalifah, 2015; Almomin and Biondi, 2012; Tang et al., 2013). All of these approaches use an extension of the gradient, similar to extended images in wave-equation migration (Sava and Fomel, 2006; Sava and Vasconcelos, 2011), to separate

tomographic and migration components by exploiting the angle between the wave vectors and to mute the reflections from the gradient. With extended images, it is also possible to implement image-domain wavefield tomography, using an objective function that penalizes energy away from zero-lag (i.e., reflections) and preserves the backscattering energy, which is mostly present at zero-lag (Diaz and Sava, 2015).

Considering these recurrent problems of crosscorrelation in RTM and FWI, we are motivated to find an imaging condition that is implemented by a simple operation between vectors that represent wavefield directionality. These vectors are defined in the 4-D space-time and can be made orthogonal for undesired events. Then, a simple dot product eliminates these events and preserves the reflectors (i.e., the image). This operation is simple to apply since it does not involve identifying specific propagation directions, as in the case for Poynting vector methods (Yoon and Marfurt, 2006).

The proposed imaging condition is also discussed by Tarantola (1984) in the context of waveform inversion using impedance as the model parameter. This imaging condition attenuates the backscattering and is related to the Laplacian filter, as shown by other authors (Brandsberg-Dahl et al., 2013; Douma et al., 2010; Pestana et al., 2013; Sun and Wang, 2013; Whitmore and Crawley, 2012). Although more general in nature, the imaging condition is ideally suited for backscattering filtering, as discussed later in this paper.

We start by reviewing the theory of energy conservation in 4-D space-time in order to develop the physical explanation of the proposed imaging condition. Then, we show how this imaging condition can be applied to RTM for attenuating the backscattering artifacts and to FWI for obtaining the tomographic term, free of reflection artifacts.

2.2 Reverse-time migration

In this section, we develop the theoretical aspects of the proposed imaging condition. We describe the conventional imaging condition as an inner product between source and receiver wavefields at each spatial location. Then, we formulate an alternative imaging condition based on the mechanical energy of the extrapolated wavefields. Appropriately

modifying the inner product enables us to use it as an imaging condition to attenuate certain reflection angles, and consequently, to attenuate backscattering artifacts from RTM images. Conversely, for transmission FWI, we attenuate the contribution of waves propagating at arbitrary angles and preserve the waves which propagate along the same paths.

2.2.1 The L_2 norm and the conventional imaging condition

For a given seismic experiment with index e, consider a wavefield $U(e, \mathbf{x}, t)$ as a solution to the acoustic wave-equation

$$\ddot{U} - v^2 \nabla^2 U = f \ , \tag{2.1}$$

where $v(\mathbf{x})$ is the medium velocity, the superscript dot indicates time differentiation, and $f(e, \mathbf{x}, t)$ is the source function. If we, for example, try to evaluate how close to one another two wavefields are, a global measure of wavefield strength is of interest in wavefield imaging. Considering U is real-valued, we can characterize the strength of the wavefield by the L_2 norm

$$\|U\|^2 = \sum_{e,\mathbf{x},t} U^2 \ . \tag{2.2}$$

An application of this norm in wavefield imaging is present in data-domain wavefield tomography, where it is used to minimize the wavefield difference at the recorded data locations. Another application is in image-domain wavefield tomography, where the norm is used to minimize the energy away from zero lag in extended images (Yang and Sava, 2015). In linear algebra, a norm is also defined as the inner product of a vector with itself (Jain et al., 2004). Hence, one can define an L_2 inner product between the two wavefields $U(e, \mathbf{x}, t)$ and $V(e, \mathbf{x}, t)$ as

$$\langle U, V \rangle = \sum_{e,\mathbf{x},t} UV \ . \tag{2.3}$$

A common application of this L_2 inner product in wavefield imaging is to compare source and receiver wavefields $U(\mathbf{x}, t)$ and $V(\mathbf{x}, t)$, respectively, and form an image $I(\mathbf{x})$ of the

subsurface:

$$I = \sum_{e,t} UV \ . \tag{2.4}$$

Note that equation 2.4 is commonly known as the conventional imaging condition (CIC), forming an image at every location where the wavefields coexist in space and time. However, the propagation directions of the different wavefields are not taken into account when forming the image. Consequently, the resulting image contains backscattering artifacts, which occur wherever source and receiver wavefields propagate along the same path. We illustrate this idea with the simple 2-D theoretical experiment depicted in Figure 2.1. The rays from source and receiver wavefields are represented in the space-time continuum. When they backscatter at the reflector depth ($z = 2.5$ km) (Figure 2.1(a) and Figure 2.1(b)), the CIC (dashed lines in Figure 2.1(c)) forms an image at all locations above the reflector where the wavefields coexist.

This imaging failure stems from the fact that the imaging condition does not account for the wavefield propagation direction. As indicated earlier, alternative imaging conditions attempt to address this challenge. In the following section, we use energy conservation laws and alternative wavefield norms to account for the wavefield propagation direction and derive a new imaging condition that exploits not only the wavefield position and timing, but also its orientation.

2.2.2 The energy norm and the proposed imaging condition

One can define a measure of energy for a solution to the acoustic homogeneous wave-equation within a spatial domain Ω (Evans, 1997; McOwen, 2003):

$$E(t) = \frac{1}{2} \int\limits_{\Omega} \left[\dot{U}^2 + v^2 \left| \nabla U \right|^2 \right] d\mathbf{x} \ . \tag{2.5}$$

The time derivative term corresponds to the kinetic energy of the wavefield, and the spatial gradient term corresponds to its potential energy. The wavefield energy is conserved over time as seen by taking the derivative of equation 2.5 with respect to time:

$$\frac{1}{2}\frac{d}{dt}\int\limits_{\Omega}\left[\dot{U}^2+v^2\left|\nabla U\right|^2\right]d\mathbf{x}= \int\limits_{\Omega}\left[\dot{U}\ddot{U}+v^2\nabla U\cdot\nabla\dot{U}\right]d\mathbf{x}\,. \tag{2.6}$$

Then, we apply the chain rule in the second term on the right-hand side of equation 2.6:

$$\begin{aligned}\int\limits_{\Omega}\left[\nabla U\cdot\nabla\dot{U}\right]d\mathbf{x} &= \int\limits_{\Omega}\nabla\cdot\left(\dot{U}\nabla U\right)d\mathbf{x}\\ &- \int\limits_{\Omega}\left(\dot{U}\nabla^2 U\right)d\mathbf{x}\,.\end{aligned} \tag{2.7}$$

The first integral on the right-hand side can be turned into a surface integral by the Divergence Theorem. Assuming homogeneous boundary conditions, i.e., the wavefield and its derivatives vanish on the boundary, we have

$$\int\limits_{\Omega}\nabla\cdot\left(\dot{U}\nabla U\right)d\mathbf{x}=\int\limits_{\delta\Omega}\dot{U}\nabla U d\mathbf{x}=0\,. \tag{2.8}$$

Substituting the remaining term from equation 2.7 into equation 2.6 yields

$$\dot{E}(t)=\frac{1}{2}\int\limits_{\Omega}\dot{U}\left(\ddot{U}-v^2\nabla^2 U\right)d\mathbf{x}=0\,, \tag{2.9}$$

for a wavefield that satisfies the homogeneous wave-equation in equation 2.1, thus indicating that the total energy of the wavefield is conserved.

A norm and an inner product in a vector space can be defined if they result in a scalar quantity and have linear properties. The energy norm is defined in this context as (Tanushev et al., 2009; Zeidler, 1999)

$$\left\|U\right\|_E^2=\sum_{e,\mathbf{x},t}\left[\dot{U}^2+v^2\left|\nabla U\right|^2\right]\,, \tag{2.10}$$

and the respective inner-product for two wavefields $U\left(e,\mathbf{x},t\right)$ and $V\left(e,\mathbf{x},t\right)$ is

$$\left\langle U,V\right\rangle_E=\sum_{e,\mathbf{x},t}\left(\dot{U}\dot{V}+v\nabla U\cdot v\nabla V\right)\,. \tag{2.11}$$

Note that the inner-product in equation 2.11 is composed of the dot product between the gradient vectors of the wavefields scaled by the velocity (v), plus the product of their time derivatives. The time dimension provides an additional derivative component beyond the components of the spatial gradient. Thus, a wavefield $U(\mathbf{x}, t)$ can be represented in an Euclidean space with spatial coordinates $\mathbf{x} = \{x, y, z\}$ and an additional coordinate vt, assuming a locally constant velocity. The gradient of U in this four-dimensional space can be defined as follows:

$$\left(v\frac{\partial U}{\partial x}, v\frac{\partial U}{\partial y}, v\frac{\partial U}{\partial z}, \dot{U}\right) \ . \tag{2.12}$$

Notice that the first 3 components of this vector form the conventional spatial gradient of the wavefield. The fourth component contains a time derivative, which is related to the temporal forward or backward character of the wavefield. Therefore, this vector indicates the space and time directionality of the wavefield at a particular position and time. This notion of a four-dimensional gradient is used in other research areas, such as special relativity and wave theory, with the following compact notation (Chappel et al., 2010; Feynman et al., 1964):

$$\Box U = \left(v\nabla U, \dot{U}\right) \ . \tag{2.13}$$

We can rewrite equations 2.10 and 2.11 using the dot product between such four-dimensional vectors:

$$\|U\|_E^2 = \|\Box U\|^2 \tag{2.14}$$

$$\langle U, V\rangle_E = \langle \Box U, \Box V\rangle \ . \tag{2.15}$$

If the inner product in equation 2.11 is evaluated at each spatial location, and the time-reversal aspect of the receiver wavefield is considered, which means this wavefield is oriented backward in time ($V(e, \mathbf{x}, T - t)$), we can define an imaging condition as

$$
\begin{aligned}
I_E &= \sum_{e,t} \Box U \cdot \Box V \ , \\
&= \sum_{e,t} \left(\dot{U}\dot{V} + v\nabla U \cdot v\nabla V \right) \ , \qquad (2.16)
\end{aligned}
$$

The energy imaging condition forms an image at every location where the dot product between the vectors $\Box U$ and $\Box V$ is nonzero. Notice that the time derivatives should be evaluated in reverse time, considering V is generated by an adjoint wave-equation operator. Figure 2.2 shows $\Box U$ and $\Box V$ for the theoretical experiment depicted in Figure 2.1. These figures show that these vectors describe the wavefield propagation direction in this space-time continuum. Notice that these vectors are not orthogonal for the backscattering events using the imaging condition in equation 2.16, and we need to slightly change the imaging condition for the purpose of preserving only the reflection information. In order to remove certain undesired events, such as backscattering artifacts, one can properly use this imaging condition to make their respective vectors $\Box U$ and $\Box V$ orthogonal to each other. In fact, this idea can be implemented to attenuate any event with a certain bisection angle.

2.2.3 Wavefield orientation in the imaging condition

Source and receiver wavefields can be decomposed in plane waves, which leads us to the reflection angle definition: the angle between the wavenumber vector of the plane wave and the normal to the reflector. For a given experiment, the Fourier transform of the wavefield is a function of the wavenumber vector and frequency: $\tilde{U}(e, \mathbf{k}, \omega)$. Using U and V transformed to the Fourier domain, one can apply the conventional imaging condition

$$
I(\mathbf{k}) = \sum_{e,\omega} \tilde{U}\tilde{V^*} \ , \qquad (2.17)
$$

where $*$ is the complex conjugate operator in frequency. The energy imaging condition uses the vectors $\Box U$ and $\Box V$ in the time domain. In the Fourier domain, these vectors can be defined in the same way as shown in equation 2.13, but using the derivative operators with respect to frequency and wavenumber components:

$$\begin{aligned}
\widetilde{\Box U} &= \left(ivk_x\tilde{U}, ivk_y\tilde{U}, ivk_z\tilde{U}, -i\omega\tilde{U}\right) \\
&= i\left(v\mathbf{k}_s, -\omega\right)\tilde{U}\ , \qquad (2.18) \\
\widetilde{\Box V} &= \left(ivk_x\tilde{V}^*, ivk_y\tilde{V}^*, ivk_z\tilde{V}^*, +i\omega\tilde{V}^*\right) \\
&= i\left(v\mathbf{k}_r, +\omega\right)\tilde{V}^*\ , \qquad (2.19)
\end{aligned}$$

considering that the adjoint derivative for V is the opposite to the forward derivative in the Fourier domain. Therefore, the dot product between $\widetilde{\Box U}$ and $\widetilde{\Box V}$ is

$$\begin{aligned}
\widetilde{\Box U}\cdot\widetilde{\Box V} &= \left[-v^2\left(\mathbf{k}_s\cdot\mathbf{k}_r\right)+\omega^2\right]\tilde{U}\tilde{V}^* \\
&= \left[-v^2||\mathbf{k}_s||||\mathbf{k}_r||\cos 2\theta+\omega^2\right]\tilde{U}\tilde{V}^*, \qquad (2.20)
\end{aligned}$$

where 2θ is the reflection aperture angle and also the angle between the spatial gradient vectors. Using the dispersion relation

$$||\mathbf{k}_s|| = ||\mathbf{k}_r|| = \frac{\omega}{v} \qquad (2.21)$$

in equation 2.20, leads to

$$\widetilde{\Box U}\cdot\widetilde{\Box V} = \left[-\omega^2\cos 2\theta+\omega^2\right]\tilde{U}\tilde{V}^*\ . \qquad (2.22)$$

In equation 2.22, in order to attenuate a certain reflection of angle θ_c, we need to apply a scaling factor to the second term (product of the time derivatives of the wavefields), thus nullifying the term in the brackets:

$$\begin{aligned}
\widetilde{\Box U}\cdot\widetilde{\Box V} &= \left[-\omega^2\cos 2\theta+\omega^2\cos 2\theta_c\right]\tilde{U}\tilde{V}^* \\
&= 0\ ,\ \text{if}\ \theta=\theta_c\ . \qquad (2.23)
\end{aligned}$$

Therefore, in the Fourier domain, the imaging condition with this angle factor is

$$\begin{aligned}
I_E(\mathbf{k}) &= \sum_{e,\omega}\widetilde{\Box U}\cdot\widetilde{\Box V} \\
&= \sum_{e,\omega}\left[\omega^2\cos 2\theta_c - v^2\left(\mathbf{k}_s\cdot\mathbf{k}_r\right)\right]\tilde{U}\tilde{V}^*\ . \qquad (2.24)
\end{aligned}$$

In the space-time domain, we can modify the imaging condition in equation 2.16 by including the angle factor:

$$I_E = \sum_{e,t} \left(\cos(2\theta_c) \dot{U}\dot{V} + v\nabla U \cdot v\nabla V \right) \ . \tag{2.25}$$

2.2.4 Backscattering attenuation

The backscattering artifact, in particular, is not a reflection. However, its wavenumber vectors $\mathbf{k_s}$ and $\mathbf{k_r}$ are collinear and opposite, with an angle of 180° between them. The artifact can be treated as having a 90° reflection angle, which implies that $\cos 2\theta_c = -1$. Therefore, we can rewrite equation 2.25 to form an imaging condition specifically designed to attenuate the backscattering energy:

$$I_E = \sum_{e,t} \left(-\dot{U}\dot{V} + v\nabla U \cdot v\nabla V \right) \ . \tag{2.26}$$

Figure 2.2(d) shows the vectors $\Box U$ and $\Box V$ for the imaging condition in equation equation 2.26. Notice that, for the backscattering artifacts, these vectors are orthogonal, which makes their dot-product zero. This means that the backscattered energy is attenuated and reflectors are preserved if we apply the imaging condition in equation equation 2.26.

The attenuation of the backscattering artifacts is one practical benefit of the energy imaging condition over its conventional L_2 counterpart. The Laplacian operator applied on the conventional image is the most common form of backscattering filtering. The proposed imaging condition is related to the Laplacian filter by (Appendix A)

$$I_E = \frac{1}{2}\nabla^2 I_{L_2} \ . \tag{2.27}$$

Therefore, the proposed imaging condition is the general form of the filtering using the Laplacian operator for any reflection angle θ_c.

2.2.5 Amplitude and phase of the energy imaging condition

Compared to the conventional imaging condition (CIC), the angle between $\Box U$ and $\Box V$ influences the amplitude of the energy image, whereas in CIC the amplitude of the image

only depends on the strength of U and V. Using I_E from equation 2.24 for the special case when $\cos 2\theta_c = -1$, we have

$$I_E = -\sum_{e,\omega} \omega^2 \left[1 + \cos 2\theta\right] \tilde{U}\tilde{V}^* \ . \tag{2.28}$$

Following the strategy from Zhang and Sun (2009), in order to preserve the phase compared to the CIC image, one can integrate the source function and receiver data before wavefield extrapolation, which means scaling I_E by $\frac{1}{\omega^2}$in the frequency domain. The amplitude of the resulting image is not exactly equal to the amplitude in CIC due to the term depending on the reflection angle $1 + \cos 2\theta$. Only if the reflection angle is known for each time and space location of the correlated wavefields, one can multiply I_E by $\frac{-1}{\omega^2[1+\cos 2\theta]}$ to get the exact amplitude and phase of CIC. This is also true for the Laplacian filter, and we can obtain the expression from Zhang and Sun (2009) starting from equation 2.27:

$$-\sum_{\omega} 2\omega^2 \left[1 + \cos 2\theta\right] \tilde{U}\tilde{V}^* = -v^2||\mathbf{k}||^2 \sum_{\omega} \tilde{U}\tilde{V}^* \ . \tag{2.29}$$

Using the trigonometric identity

$$1 + \cos 2\theta = 2\cos^2\theta \ , \tag{2.30}$$

we obtain from equation 2.29 the following relation:

$$||\mathbf{k}||^2 = \frac{4\omega^2 \cos^2\theta}{v^2} \ , \tag{2.31}$$

which means the Laplacian filter also has a term that depends on the reflection angle θ.

Another particular case is when the energy imaging condition is used to attenuate normal-incidence reflections ($\cos 2\theta_c = 1$). Using equation 2.24 and the following trigonometric identity

$$1 - \cos 2\theta = 2\sin^2\theta \ , \tag{2.32}$$

we obtain the following pair of imaging conditions:

$$I_E(\mathbf{k}, \theta_c = 0^\circ) \quad = +2 \sum_{e,\omega} \omega^2 \sin^2 \theta \tilde{U} \tilde{V}^* \,, \tag{2.33}$$

$$I_E(\mathbf{k}, \theta_c = 90^\circ) \quad = -2 \sum_{e,\omega} \omega^2 \cos^2 \theta \tilde{U} \tilde{V}^* \,, \tag{2.34}$$

whose difference multiplied by $\frac{1}{\omega^2}$ is equivalent to the conventional image. Later in this paper, we exploit the complementary behavior of these two imaging conditions.

2.2.6 Examples

With simple synthetic examples, we illustrate the application of the proposed imaging condition. Then, we show its effectiveness with a complex model (Sigsbee).

Figure 2.3 shows a simple constant velocity experiment with a flat reflector at $z = 2$ km, and with one source and one receiver on the surface at $x = 2.5$ km and $x = 7.5$ km, respectively. As expected, the conventional image (Figure 2.3(a)) shows backscattering artifacts, which are very strong along the path at the 45° reflection angle. The Laplacian filter applied on the conventional image, Figure 2.3(b), attenuates backscattering artifacts. The energy image in Figure 2.3(c), which uses the imaging condition in equation 2.26, shows a similar result compared to Figure 2.3(b), proving the equivalency of these images for the far-field.

Figure 2.4 shows the application of the imaging condition in equation 2.25. In these images, every reflection of a certain angle is attenuated by scaling the time derivative product by $\cos(2\theta_c)$. This proves that our new imaging condition can be used to attenuate reflections for arbitrary angles. Later in this paper, we describe a specific application exploiting this generalization.

Figure 2.5 show imaging results from selected single shots using these different imaging conditions for the Sigsbee model. Stacking all individual migrated images, we obtain the migrated images in Figure 2.6. Figure 2.6(a) shows the stratigraphic velocity model that was used to generate the synthetic data for the experiment. The conventional image in

Figure 2.6(b) is masked by the low-frequency backscattered energy. The application of the energy norm imaging condition removes the low-frequency artifacts in Figure 2.6(c).

2.3 Full waveform inversion

The same methodology applied in the preceding section for migration can also be applied to waveform inversion. The gradient of the objective function (required to update the velocity) is equivalent to an RTM image of the data difference, instead of the data themselves, if the adjoint-state method is implemented (Plessix et al., 1999). We begin this section by reviewing the adjoint-state method. Then, we use the energy norm to obtain the inner product between state and adjoint variables, which is required in the calculation of the objective function gradient. Modifying the inner product properly, we are able to filter the gradient and preserve the tomographic term while attenuating the migration term.

2.3.1 Adjoint-state method

Data-domain wavefield tomography consists of comparing simulated and observed wavefields at specific data locations, improving their similarity at each iteration, and then generating an optimized velocity. The difference between these two wavefields, called the data residual, is the most common form of comparison:

$$r_d = \mathbf{W}_u(u_s - u_r) \ , \tag{2.35}$$

where $\mathbf{W}_u\,(e, \mathbf{x}, t)$ is an operator that restricts the wavefields at data locations, and $u_s\,(e, \mathbf{x}, t)$ and $u_r\,(e, \mathbf{x}, t)$ are the source and receiver wavefields, respectively. The source and receiver wavefields restricted at the receiver locations are equivalent to the synthetic and observed data, respectively. The data residual is also a function of space, time and experiment index: $r_d\,(e, \mathbf{x}, t)$. These wavefields are obtained using a proper wave equation, which can be represented by the differential operator $\mathcal{L}$ that admits the adjoint operator $\mathcal{L}^{\mathrm{T}}$ for back propagation. The equations governing the wave propagation for each one of the wavefields

are the physical constraints for the inverse problem (Sava, 2014):

$$\begin{bmatrix} \mathcal{F}_s \\ \mathcal{F}_r \end{bmatrix} = \begin{bmatrix} \mathcal{L} & 0 \\ 0 & \mathcal{L}^{\mathrm{T}} \end{bmatrix} \begin{bmatrix} u_s \\ u_r \end{bmatrix} - \begin{bmatrix} d_s \\ d_r \end{bmatrix} = \begin{bmatrix} 0 \\ 0 \end{bmatrix} , \tag{2.36}$$

where $d_s\left(e, \mathbf{x}, t\right)$ and $d_r\left(e, \mathbf{x}, t\right)$ are the source functions of the wave equations using $\mathcal{L}$ and $\mathcal{L}^{\mathrm{T}}$ at the source and receiver locations, respectively.

With a residual, we can define an objective function:

$$\mathcal{J}_{L_2} = \sum_e \frac{1}{2} ||r_d||^2_{L_2} . \tag{2.37}$$

In order to minimize the defined objective function, we need to compute its gradient with respect to model parameters. The gradient is robustly obtained by the adjoint-state method:

$$\frac{\partial \mathcal{J}}{\partial m} = -\left\langle a, \frac{\partial \mathcal{F}}{\partial m} \right\rangle , \tag{2.38}$$

where $m\left(\mathbf{x}\right)$ is the model parameter; $\mathcal{F}$ is the physical realization equation, which can be either $\mathcal{F}_s$ or $\mathcal{F}_r$ in equation 2.36; $a\left(e, \mathbf{x}, t\right)$ is the adjoint-state variable; and $\langle , \rangle$ is the inner product between the adjoint-state variable and the derivative of $\mathcal{F}$ with respect to the model parameters (Plessix, 2006).

An inner product must output a scalar quantity from two vectors and must have linear properties (Jain et al., 2004). Both inner products in L_2 or L_E norms satisfy these requirements. Therefore,

$$\frac{\partial \mathcal{J}}{\partial m} = -\left\langle a, \frac{\partial \mathcal{F}}{\partial m} \right\rangle_{L_2} = -\left(\frac{\partial \mathcal{F}}{\partial m} \right)^{\mathrm{T}} a , \tag{2.39}$$

$$\frac{\partial \mathcal{J}}{\partial m} = -\left\langle a, \frac{\partial \mathcal{F}}{\partial m} \right\rangle_{E} = -\left\langle \Box a, \Box \frac{\partial \mathcal{F}}{\partial m} \right\rangle . \tag{2.40}$$

The adjoint-state variable $a\left(e, \mathbf{x}, t\right)$ is computed using the adjoint of the wave-equation operator in either one of the equations in 2.36. The adjoint-state variable can be defined as a_s or a_r depending on which physical constraint is used from equation 2.36:

$$\begin{bmatrix} \mathcal{L}^{\mathrm{T}} & 0 \\ 0 & \mathcal{L} \end{bmatrix} \begin{bmatrix} a_s \\ a_r \end{bmatrix} = \begin{bmatrix} g_s \\ g_r \end{bmatrix} , \tag{2.41}$$

where $g_s\,(e,\mathbf{x},t)$ and $g_r\,(e,\mathbf{x},t)$ are the adjoint sources, and they are defined as the derivative of the objective function with respect to state variables. We can use equation 2.37 to obtain the adjoint sources:

$$\begin{bmatrix} g_s \\ g_r \end{bmatrix} = \begin{bmatrix} \frac{\partial \mathcal{J}}{\partial u_s} \\ \frac{\partial \mathcal{J}}{\partial u_r} \end{bmatrix} = \begin{bmatrix} +\mathbf{W}_u^{\mathrm{T}} \\ -\mathbf{W}_u^{\mathrm{T}} \end{bmatrix} r_d \ . \tag{2.42}$$

In summary, our goal is to compute the gradient by using equation 2.40 in a form that favors the tomographic term and attenuates the migration term.

2.3.2 Application of the energy norm imaging condition to preserve the tomographic term

In the previous section, we discuss the application of the energy norm imaging condition for attenuating a certain reflection angle, leading to a pair of complementary imaging conditions in equations 2.33 and 2.34. As these two images are complementary with respect to angle, the maximum value of one imaging condition is the minimum value of the other imaging condition, and vice-versa. We are interested in selecting a narrow range of reflection angles near 90°, i.e., from backscattering, diving and head waves. However, the image $I_E(\mathbf{k},\theta_c=0°)$, which has maximum amplitude at 90°, selects a broad range of reflection angles. A suitable option to make this range narrower is to apply an exponential function that has the greatest decay for angles far from 90°. The complementary image $I_E(\mathbf{k},\theta_c=90°)$ indicates how far a certain angle is from 90°. Considering this, we can define the filtered image by an exponential function applied to $I_E(\mathbf{k},\theta_c=0°)$ as

$$I_E^{tomo} = I_E(\mathbf{k},\theta_c=0°)e^{-aI_E(\mathbf{k},\theta_c=90°)} \ , \tag{2.43}$$

where I_E^{tomo} stands for the tomographic component of the image. In equation 2.43, by inserting the complementary image $I_E(\mathbf{k},\theta_c=90°)$ into the exponential function with a proper factor $a>1$, we are able to select a narrower range of reflection angles from $I_E(\mathbf{k},\theta_c=0°)$, without directly computing these angles. The image inside the exponential should be normalized, such that only the $\sin^2(\theta)$ factor is accounted for in the exponential. In equations 2.33 and 2.34, the term that depends on the reflection angle for each imaging

condition is $\sin^2(\theta)$ and $\cos^2(\theta)$, respectively. Figure 2.7 presents a plot of these terms and a plot of $\sin^2(\theta)$ with the exponential function applied. The application of the exponential function to $\sin^2(\theta)$ resembles the exponential filter application in equation 2.43.

The complementary relation found in equations 2.33 and 2.34 is also applicable for the source and receiver wavefields at each time step. The multipathing character of the wavefields causes different reflection angles to overlap in the image. Consequently, a more ideal procedure would involve applying exponential filtering in the wavefield domain, before stacking over time.

2.3.3 Examples

We investigate the efficiency of the proposed FWI gradient filtering by using a very simple model with a true velocity of 2.5 km/s. Figure 2.8 shows experiments with a geometry consisting of one source at $x = 1$ km and one receiver at $x = 5$ km, both at depth $z = 2.25$ km. The percentage of increase from the true velocity is 30%. In Figure 2.8(a), the data residual consists of two separated signals, one from the synthetic and the other from the observed direct wave. In Figure 2.8(c), the wavefield constructed from the simulated data correlates with the source wavefield along the direct path between source and receiver, thus generating the well-known low-frequency waveform inversion sensitivity kernel. Similarly, the wavefield reconstructed from the observed data correlates with the source wavefield at all locations that match the total traveltime from the source to the receiver. This correlation harms the gradient by placing an apparent reflector where it does not exist; we intend to attenuate this correlation with the proposed exponential filter by selecting only the wavefield correlations at 180°. We can apply the exponential filter either in the image domain (Figure 2.8(e)) or in the wavefield domain (Figure 2.8(g)). The filter is effective in removing the reflections, though weak energy from wide-angle reflections remain. We obtain improved results with filter applied in the wavefield domain (Figure 2.8(g)). For a similar model with a free surface, we obtain the gradients in Figures 2.8(d),2.8(f), and 2.8(h). Due to multiple paths, crosstalk artifacts are visible in the conventional gradient (Figure 2.8(d)). The filtered gradients

(Figures 2.8(f) and 2.8(h)) show decreased amplitude for wide-angle reflections both in the image and in the wavefield domains. The factor a in the exponent function is empirically chosen for all experiments using this filtering.

Figures 2.9-2.11 show a FWI experiment for the Marmousi model (Bourgeois et al., 1991). For this synthetic experiment, we use a source wavelet with maximum frequency of 9 Hz and the velocity model in Figure 2.9(a) to generate the observed data, which are recorded at every point at the surface. Then, changing the velocity for the one in Figure 2.9(b), we generate the synthetic wavefield and data. For a single shot record at position $x = 1.01$ km, we obtain the gradients using conventional imaging condition in Figure 2.10(a) and using the exponential filtering in image domain (Figure 2.10(b)) or wavefield domain (Figure 2.10(c)). The filtered gradients enhance the tomographic term created by diving waves and attenuates the migration term created by the reflections. Note that the gradient obtained through filtering in the wavefield domain resolves multipathing better than in the image domain, attenuating reflections better while preserving the tomographic term. Repeating the procedure for 27 shots, starting at $x = 0$ km and ending at $x = 6.51$ km (equally spaced by 250 m), we obtain the stacked gradients in Figure 2.11. The conventional gradient in Figure 2.11(a) contains reflectors, which are attenuated in Figures 2.11(b) and 2.11(c).

2.4 Conclusions

The energy imaging condition provides an elegant and effective procedure for attenuating backscattering artifacts in reverse-time migration; this method generates an image representing the projection of four-dimensional gradients ($\Box U$ and $\Box V$) onto one-another. Our new imaging condition also offers a physical explanation for the effectiveness of the Laplacian operator in attenuating events corresponding to waves propagating along the same path. The imaging condition can also be used to attenuate an arbitrary reflection angle. Future work would involve exploiting this flexibility of the imaging condition for attenuating any reflection angle to obtain an extended image in the angle domain. The new imaging condition can also be used to generate complementary images as a function of incidence and

reflection angles. This complementary property between the images enables us to filter the FWI gradient in order to attenuate its reflection components and favor the transmission (tomographic) component.

2.5 Acknowledgments

We would like to thank sponsor companies of the Consortium Project on Seismic Inverse Methods for Complex Structures, whose support made this research possible. The reproducible numeric examples in this paper use the Madagascar open-source software package (Fomel et al., 2013) freely available from http://www.ahay.org.

2.6 Appendix

The appendices below elucidate specific points of this current chapter.

2.6.1 Relation with the Laplacian operator

One can show that the imaging condition in equation 2.26 is equivalent to the Laplacian filter under certain assumptions. Rewriting the imaging condition in equation 2.26 with continuous wavefields along time yields

$$I_E = \int_0^T \left[-\dot{U}\dot{V} + v\nabla U \cdot v\nabla V \right] dt \;, \tag{2.44}$$

where the source wavefield is oriented forward in time: $U(\mathbf{x}, t)$; and the receiver wavefield is oriented backward in time: $V(\mathbf{x}, T-t)$. Using integration by parts in the first term of the integrand, we have

$$\begin{aligned} -\int_0^T \dot{U}\dot{V} dt &= -\left[V\dot{U} \right]_0^T + \int_0^T U\ddot{V} dt \\ &= -\left[U\dot{V} \right]_0^T + \int_0^T V\ddot{U} dt \;. \end{aligned} \tag{2.45}$$

Assuming homogeneous initial and final conditions, the wavefields and their derivatives evaluated at $t = 0$ and $t = T$ become zero. Substituting the remaining terms in equation 2.44 gives

$$I_E = \int_0^T \left[\frac{1}{2} V \ddot{U} + \frac{1}{2} U \ddot{V} + v \nabla U \cdot v \nabla V \right] dt \ . \tag{2.46}$$

In the far field, the source and receiver wavefields satisfy the homogeneous acoustic wave-equation. Therefore,

$$I_E = \frac{1}{2} \int_0^T \left[v^2 V \nabla^2 U + v^2 U \nabla^2 V + 2 v \nabla U \cdot v \nabla V \right] dt \ . \tag{2.47}$$

Scaling this imaging condition by $\frac{1}{v^2}$, we obtain

$$I_E = \frac{1}{2} \int_0^T \left[V \nabla^2 U + U \nabla^2 V + 2 \nabla U \cdot \nabla V \right] dt \ . \tag{2.48}$$

Using calculus, we obtain

$$\nabla^2 UV = V \nabla^2 U + U \nabla^2 V + 2 \nabla U \cdot \nabla V \ , \tag{2.49}$$

and therefore

$$I_E = \frac{1}{2} \nabla^2 \int_0^T UV dt = \frac{1}{2} \nabla^2 I_{L_2} \ , \tag{2.50}$$

which means the energy imaging condition I_E is equivalent to the Laplacian applied on the conventional image I_{L_2} by a scaling factor of $^1/_2$.

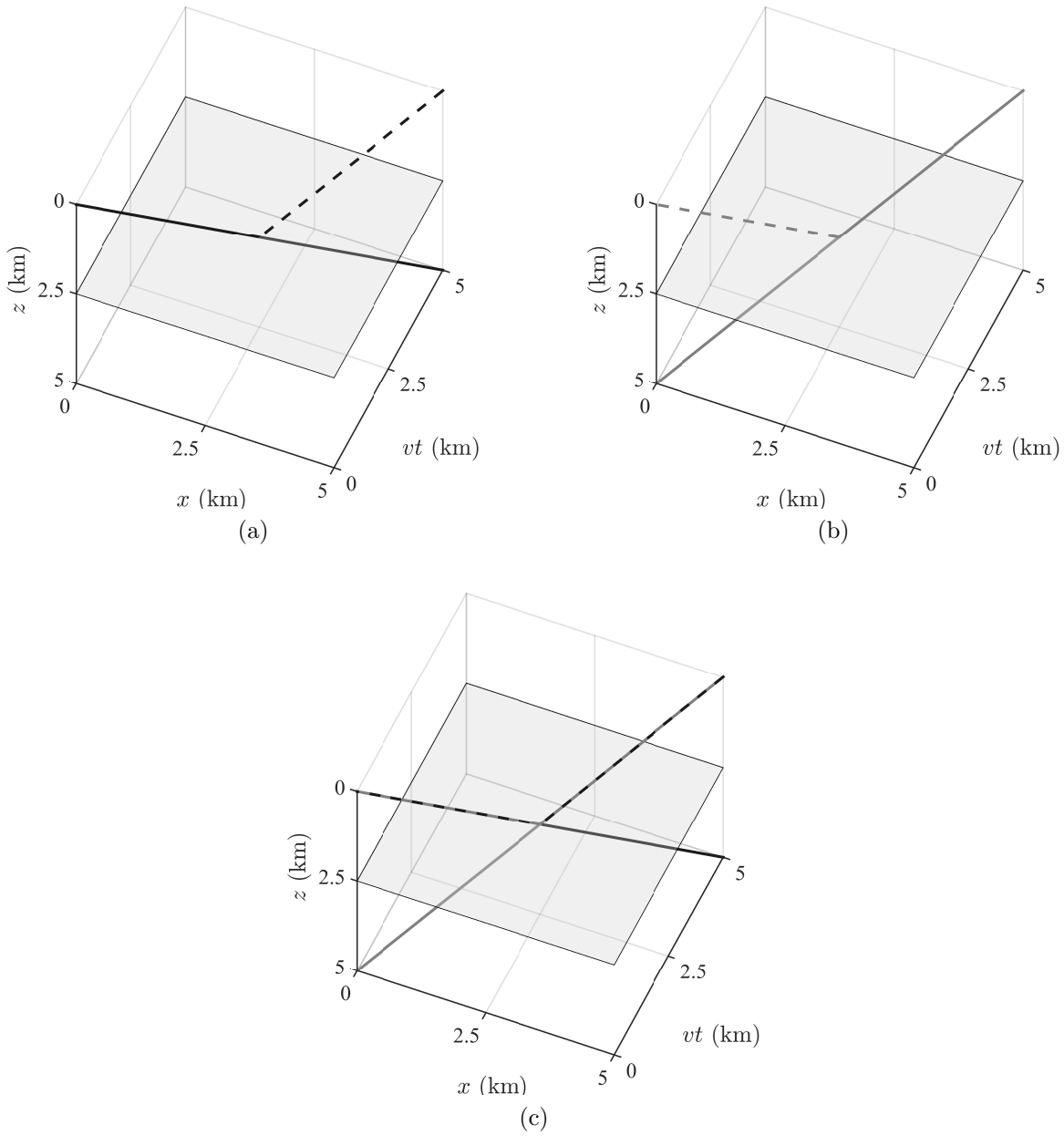


Figure 2.1: Schematic representation of (a) the source wavefield, (b) the receiver wavefield, and (c) conventional imaging, for a horizontal reflector at z=2.5 km in a 2-D experiment. The backscattered waves from source and receiver wavefields coexist in space and time and, consequently, overlap in the conventional image.

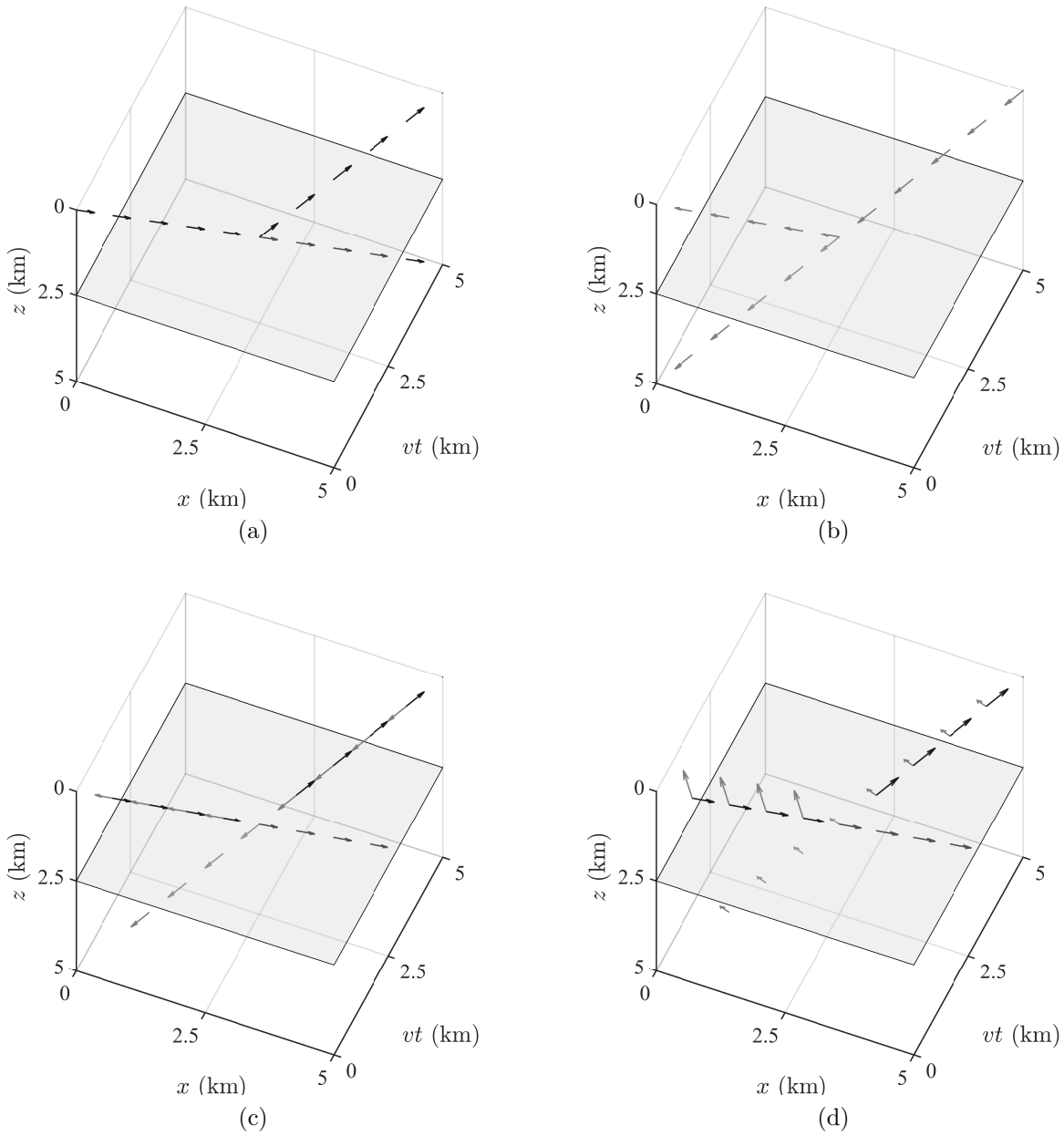


Figure 2.2: Schematic representation of the vector fields (a) $\square U$, (b) $\square V$, (c) the vector fields plotted together and (d) the imaging condition in equation 2.26. Notice that in (d), the backscattering events are characterized by orthogonal vectors $\square U$ and $\square V$, while the reflections are characterized by non-orthogonal vectors $\square U$ and $\square V$.

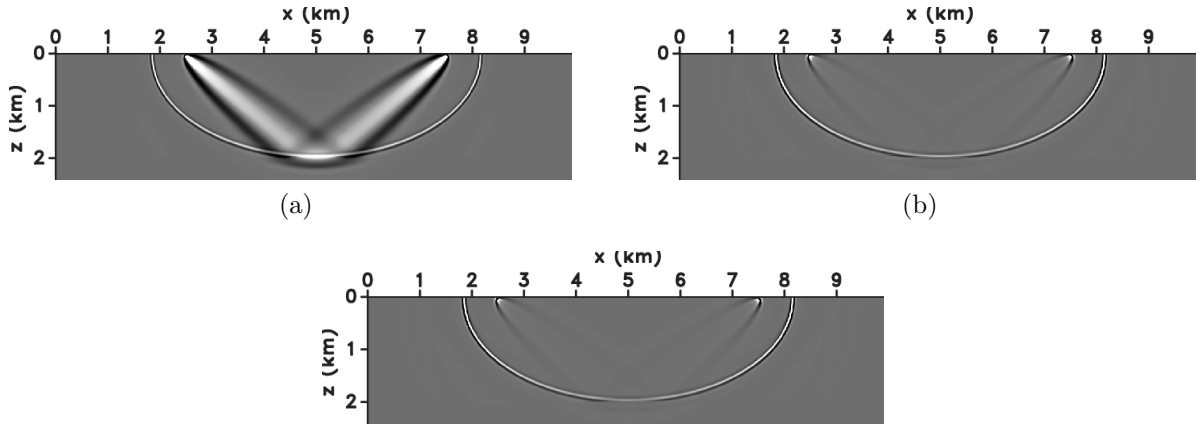


Figure 2.3: Experiment with a flat reflector, one source and one receiver on the surface at the locations $x = 2.5$ km and $x = 7.5$ km, respectively: (a) conventional imaging condition and (b) with Laplacian filter applied, and (c) energy norm imaging condition.

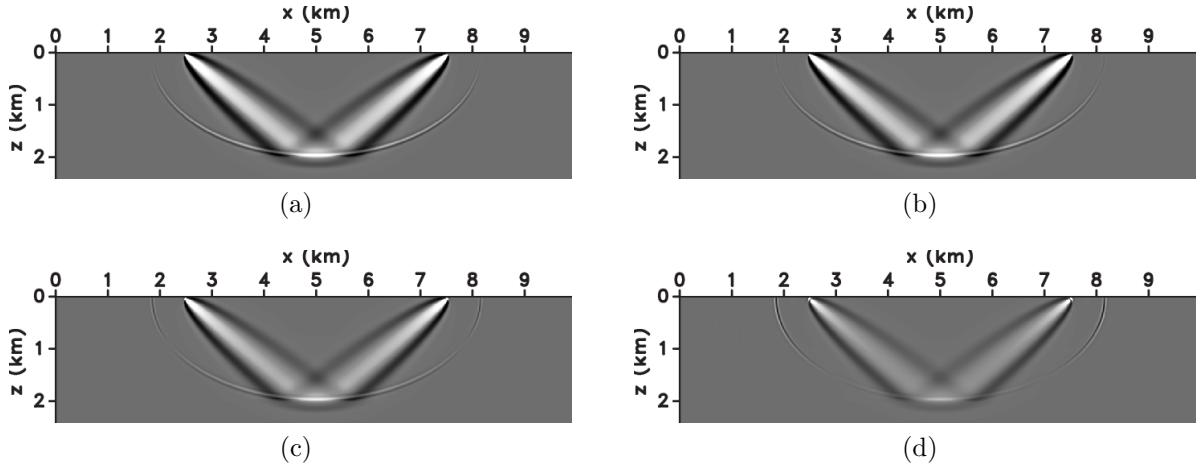


Figure 2.4: Same experiment geometry and model from Figure 2.3, but using the energy norm imaging condition to attenuate certain reflection angles: (a) normal-incidence reflections, (b) 15° reflections, (c) 30° reflections, and (d) 45° reflections.

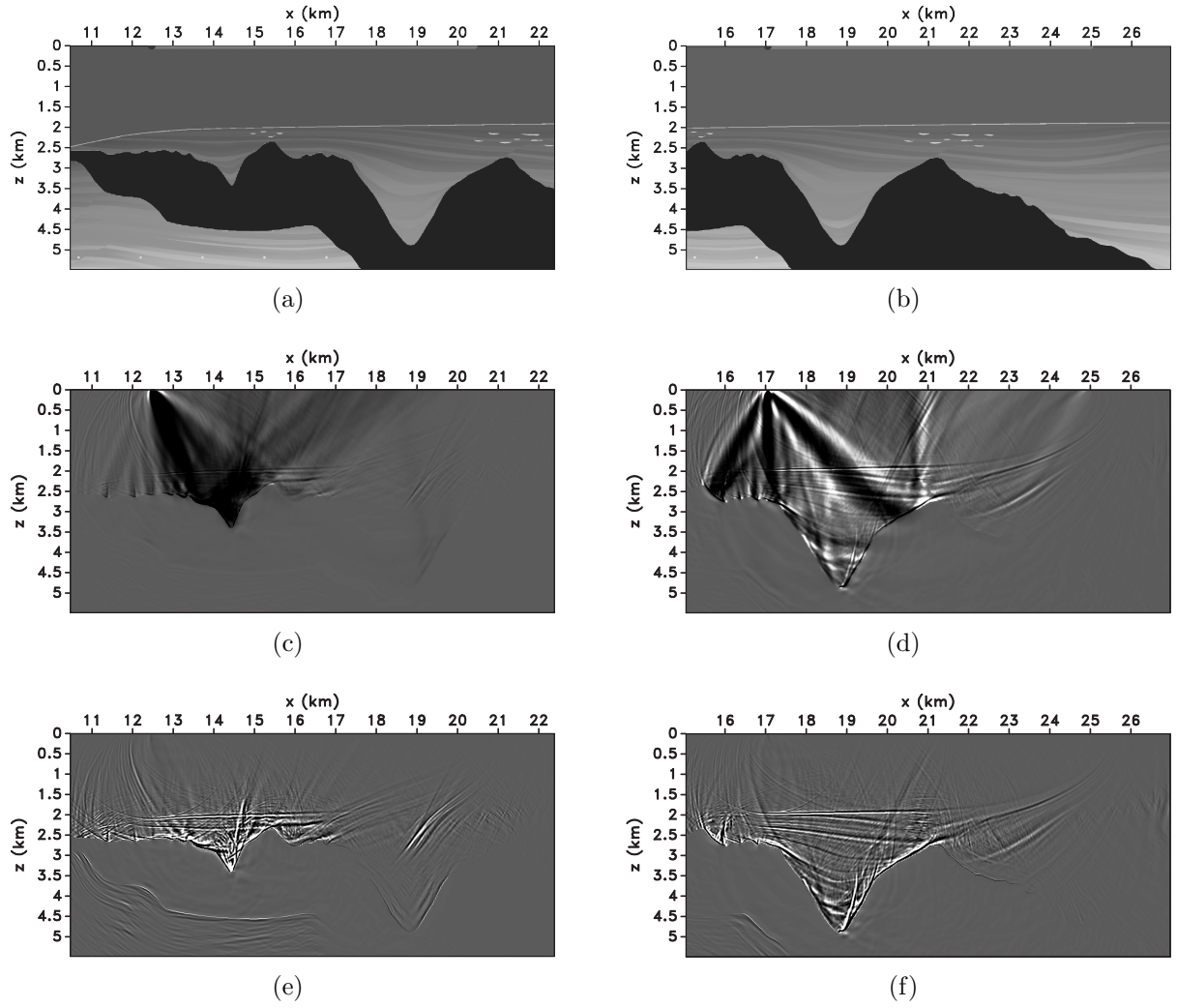
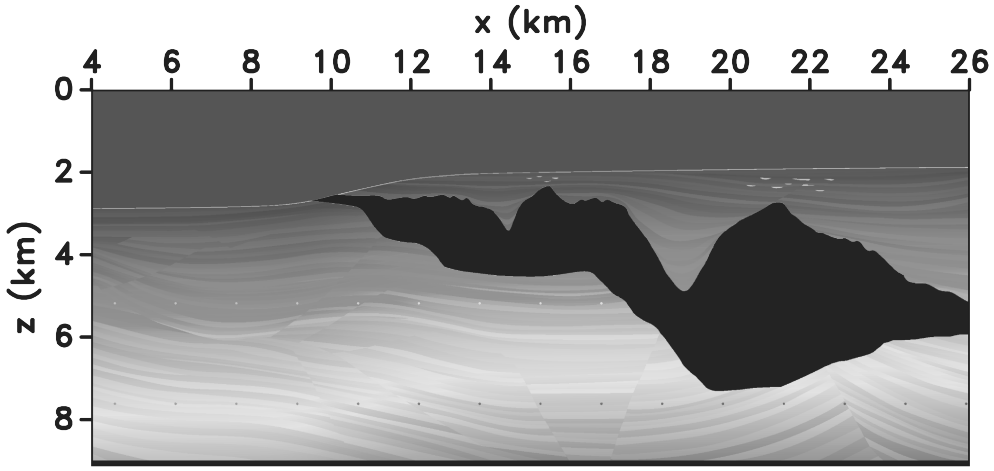
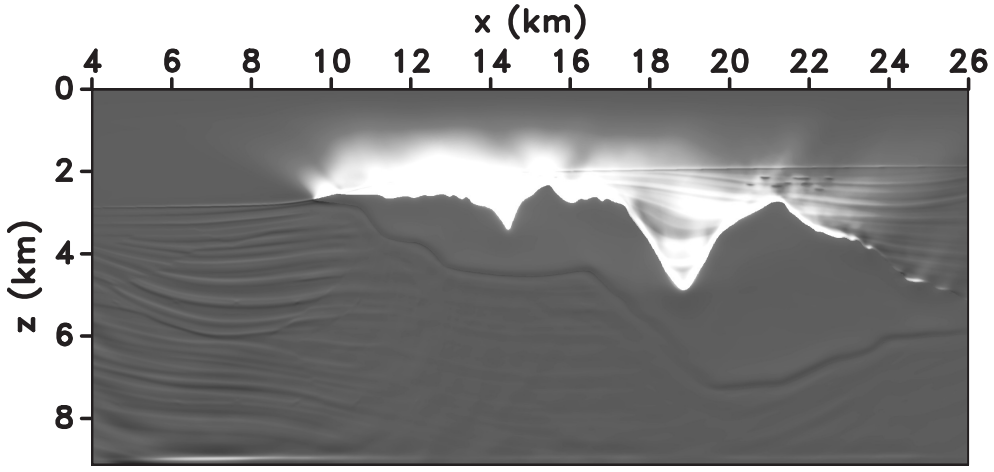


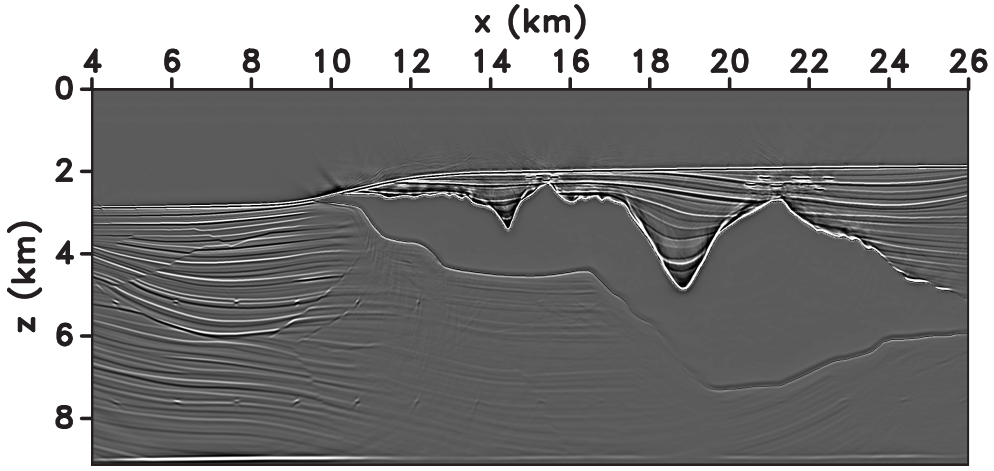
Figure 2.5: Single-shot Sigsbee migrations. (a) and (b): sections of the stratigraphic velocity model overlaid by source and receiver positions (dark point and grey line at $x = 0$ km, respectively); (c) and (d): conventional images; (e) and (f) energy images.



(a)



(b)



(c)

Figure 2.6: Mutiple-shot Sigsbee migration: (a) stratigraphic velocity model, (b) conventional image, and (c) energy image.

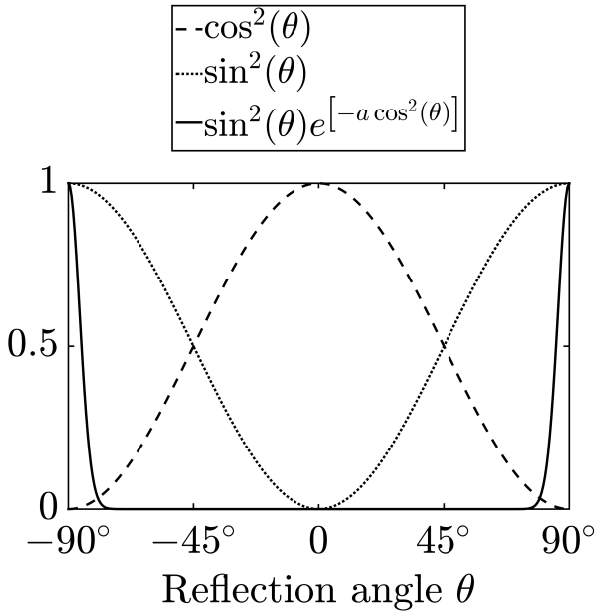


Figure 2.7: Plots of the angle-dependent functions of the imaging conditions in equations 2.33 (dotted line) and 2.34 (dashed line). An exponential in function of $\cos^2(\theta)$ and scaling factor $a = 100$ is applied on $\sin^2(\theta)$ (solid line).

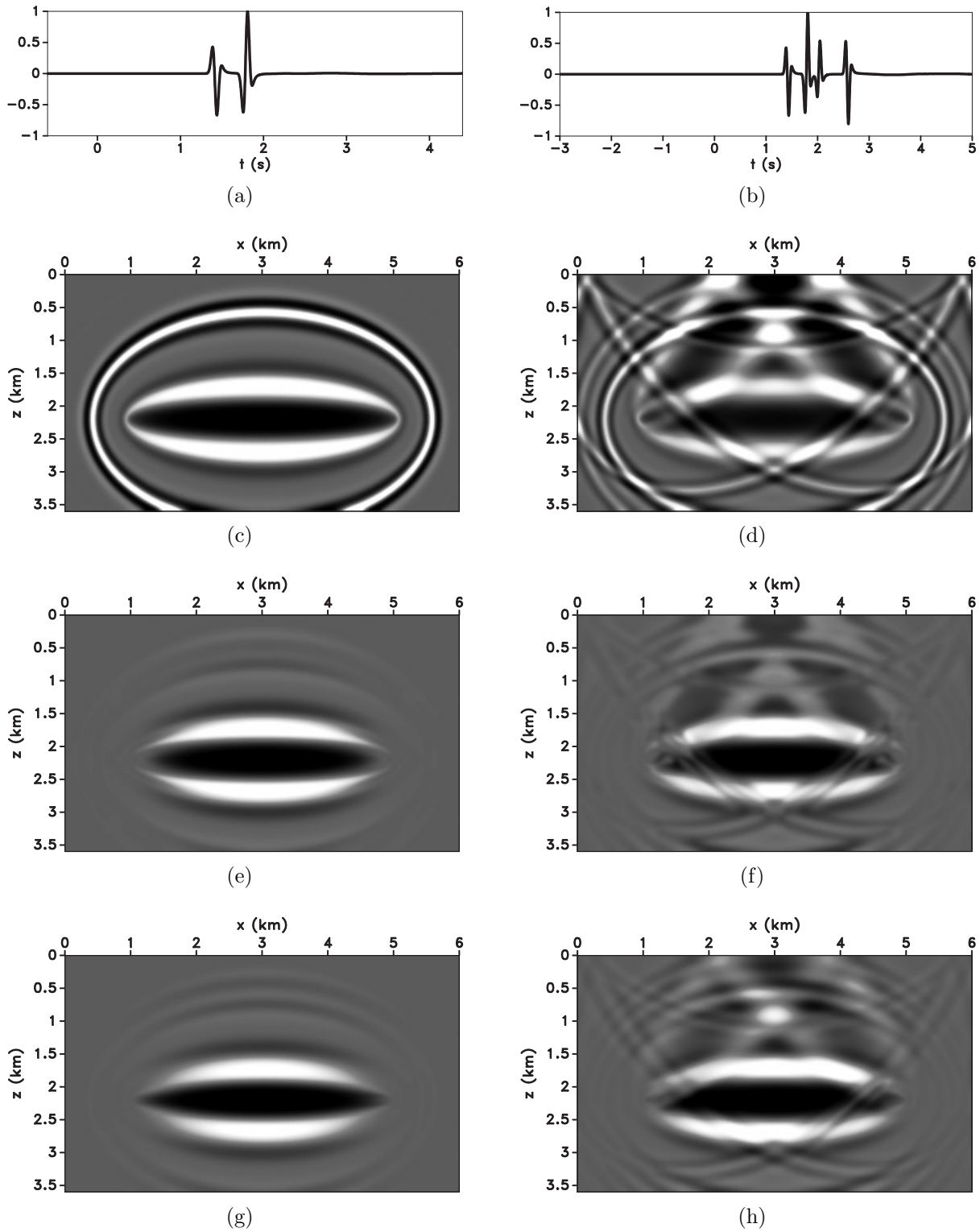
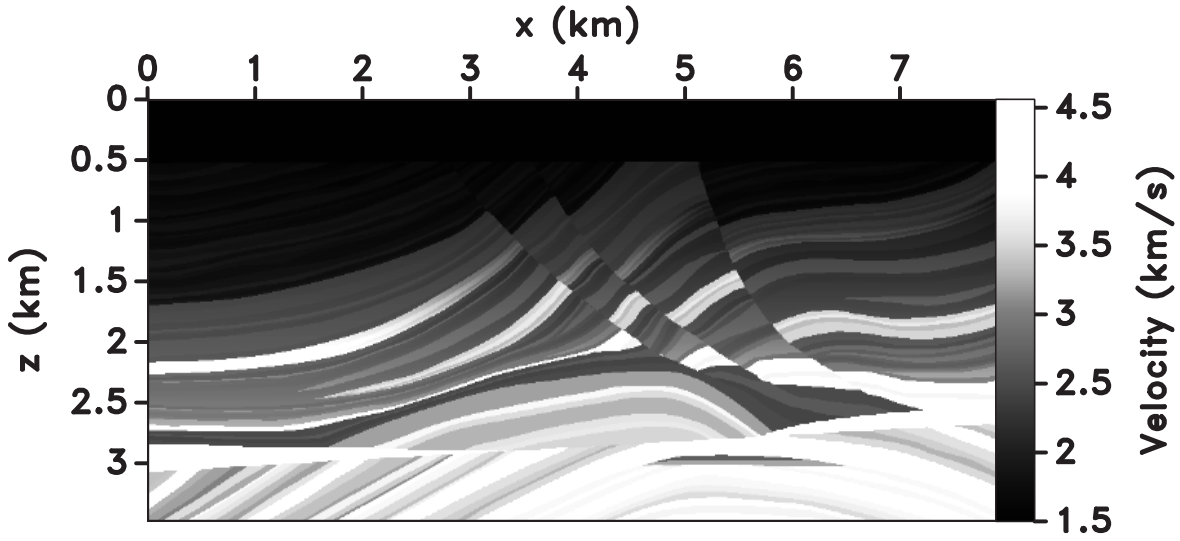
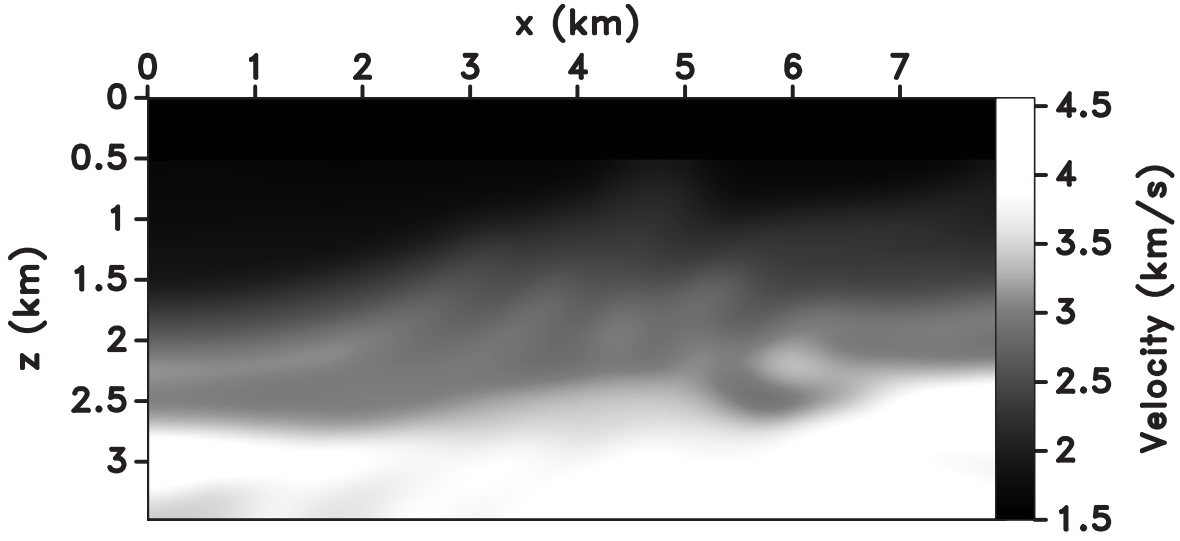


Figure 2.8: Simple FWI experiments with an increase of 30% in velocity from the true model, without and with a free surface at $x = 0$ km, respectively: (a)/(b) Data residual, (c)/(d) conventional FWI gradient, (e)/(f) energy filtered FWI gradient, with the exponential filter applied on the image, and (g)/(h) on the wavefields. Most of the reflection artifacts are attenuated by the filtering.

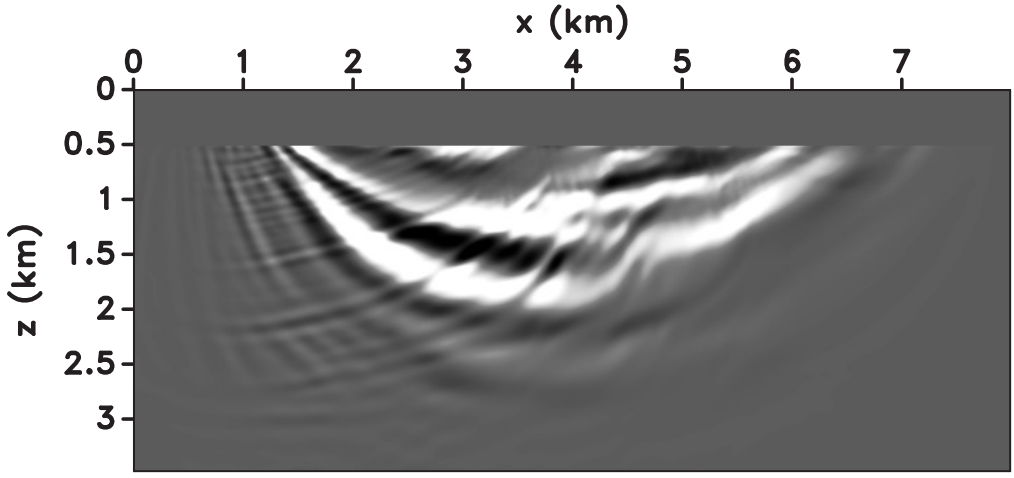


(a)

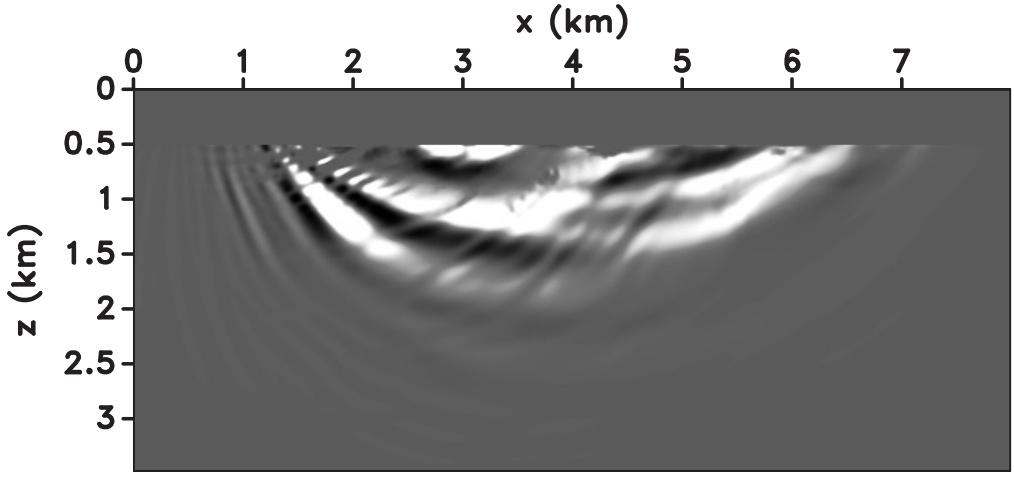


(b)

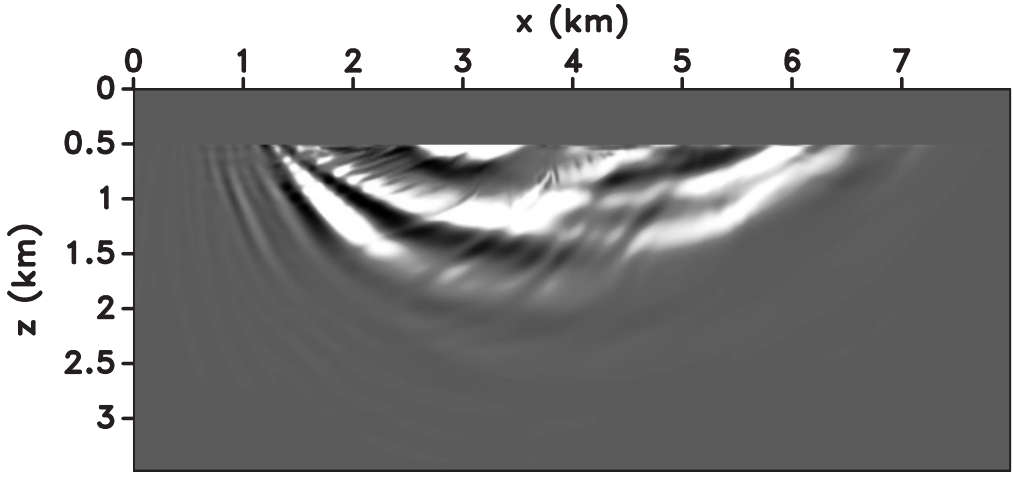
Figure 2.9: Velocity models used in the Marmousi FWI experiment: (a) True velocity and (b) Initial velocity.



(a)

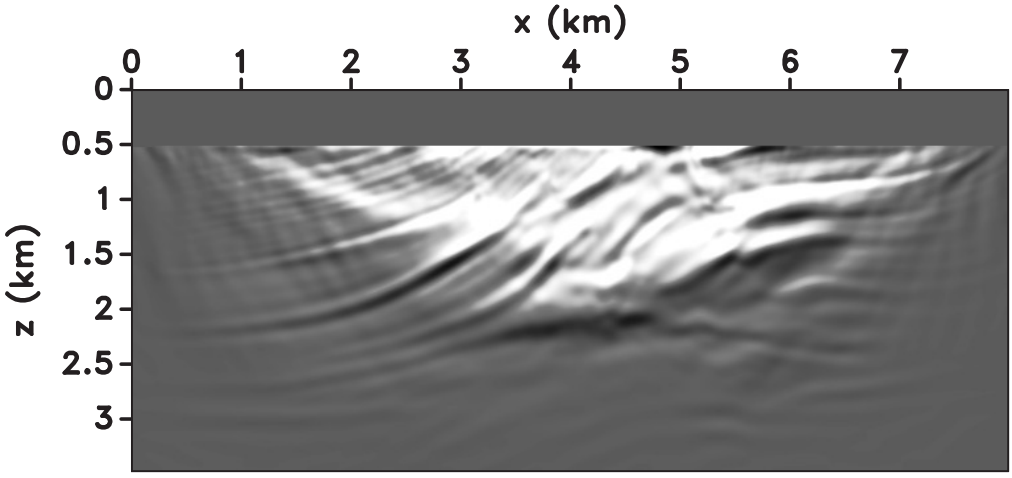


(b)

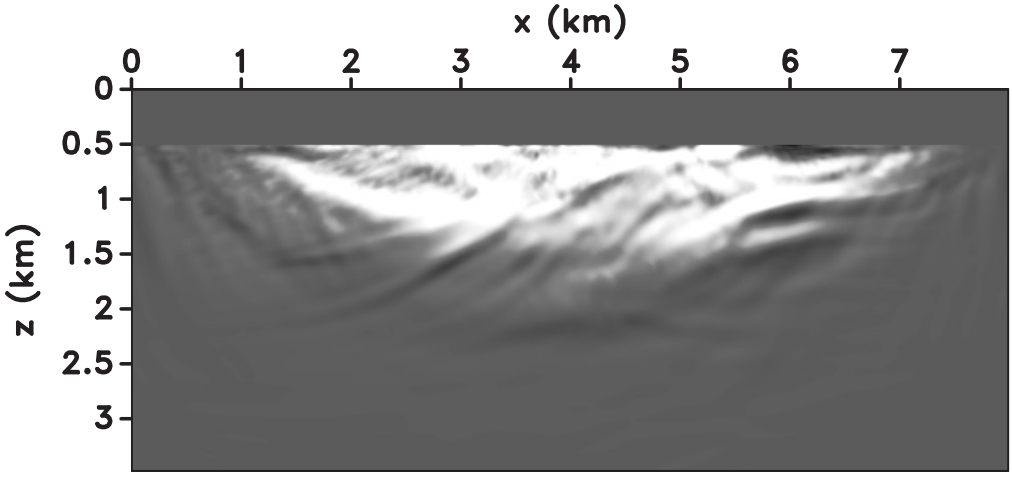


(c)

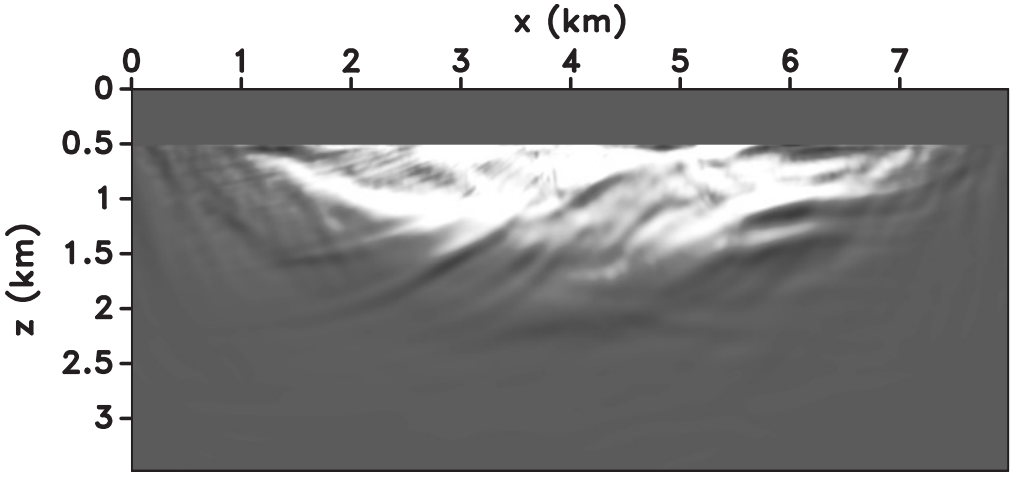
Figure 2.10: FWI gradients for a single shot at the first iteration: (a) conventional FWI gradient, (b) energy filtered FWI gradient, with the exponential filter applied on the image, and (c) on the wavefields.



(a)



(b)



(c)

Figure 2.11: FWI gradients for stacked shots at the first iteration: (a) conventional FWI gradient, (b) energy filtered FWI gradient, with the exponential filter applied on the image, and (c) on the wavefields.

CHAPTER 3

ELASTIC WAVEFIELD IMAGING USING THE ENERGY NORM

Submitted to Geophysics for publication

Daniel Rocha[*,1], Nicolay Tanushev[2] and Paul Sava[1]

From the elastic wave equation and the energy conservation principle, we derive an *energy norm* that is applicable to imaging with elastic wavefields. Extending the concept of the norm to an inner product enables us to compare two related wavefields. For example, the inner product of source and receiver wavefields at each spatial location leads to an imaging condition. This new imaging condition outputs a single image representing the total reflection energy, and contains individual terms related to the kinetic and potential energy (strain energy) from both extrapolated wavefields. An advantage of the proposed imaging condition compared to alternatives is that it does not suffer from polarity reversal at normal incidence, as do conventional images obtained using converted waves. Our imaging condition also accounts for the directionality of the wavefields in space and time. Based on this information, we modify the imaging condition for attenuation of backscattering artifacts in elastic reverse-time migration images. Numerical experiments show the improved quality of the energy images compared to their conventional counterparts, and the effectiveness of the imaging condition in attenuating backscattering artifacts even in media characterized by high spatial variability.

3.1 Introduction

Seismic wavefield imaging is usually implemented using the acoustic wave-equation, based on the inaccurate assumption that only compressional waves propagate in the subsurface.

* Corresponding author. Direct correspondence to drocha@mines.edu
[1] Center for Wave Phenomena, Colorado School of Mines, 924 16th St., Golden, CO 80401
[2] Z-Terra Inc., 17171 Park Row Dr. #247, Houston, TX 77084

The search for more authentic images and for subsurface information such as fracture distribution drives the development of wavefield imaging using the elastic wave equation. Multicomponent seismic recording and improved computer resources have made elastic wavefield imaging possible (Chen and Huang, 2014; Denli and Huang, 2008; Duan and Sava, 2014a,b; Yan and Sava, 2011; Yan and Xie, 2012).

For both acoustic and elastic cases, wave-equation migration consists of two steps: (1) wavefield extrapolation in the subsurface, using data recorded at the surface or the known source function, and (2) the application of an imaging condition for the purpose of extracting the Earth's reflectivity from wavefields (Claerbout, 1971; Dellinger and Etgen, 1990; Yan and Sava, 2009). If a two-way elastic wave equation is used in the wavefield extrapolation step, followed by an imaging condition representing zero-lag crosscorrelation between the wavefields, the imaging procedure is called elastic reverse time migration (RTM) (Chang and McMechan, 1987; Hokstad et al., 1998). In recent years, many elastic imaging conditions have been proposed by exploiting the multicomponent aspect of the elastic wavefield and the possibility of decomposing the displacement fields into P- and S-wave modes (Duan and Sava, 2014a; Etgen, 1988; Yan and Sava, 2007; Yan and Xie, 2010; Zhe and Greenhalg, 1997). Correlating the displacement fields for each component of the source and receiver wavefields leads to images with a mixture of P- and S-wave modes, thus making interpretation challenging. In addition, the nine images generated by this kind of imaging condition represent another difficulty for interpretation in 3-D. Alternatively, if the displacement wavefields are separated into P and S waves using Helmholtz decomposition, one can correlate specific wave modes from source and receiver wavefields (Etgen, 1988; Yan and Sava, 2007). Another issue for both displacement and potential imaging conditions is polarity reversal, which occurs in elastic images due to changes in the elastic wavefield polarization. Specifically, converted waves change sign due to the different orientation of P- and S-polarization vectors in relation to subsurface interfaces. For isotropic media, this polarity reversal occurs at normal incidence (Balch and Erdermir, 1994), which enables polarity reversal corrections

either after angle-domain imaging (Yan and Sava, 2008) or by exploiting the relationship between incidence directions and reflector orientation (Duan and Sava, 2014a).

In addition to the issue of polarity reversal, elastic images have the disadvantage of containing artifacts that degrade image quality. As shown in detail elsewhere (Duan and Sava, 2014a; Yan and Sava, 2007), injecting elastic data into a model (implementing back propagation) creates the so-called "fake modes" during the wavefield extrapolation step, and leads to artifacts during the application of an imaging condition. These artifacts might be present even after stacking, masking weak reflections in the final image (Duan and Sava, 2014b). A second type of artifact appears if the elastic model contains sharp interfaces. In this case, backscattered reflections occur during the wavefield extrapolation step, and the application of conventional imaging conditions create low-wavenumber artifacts in the image (Chen and Huang, 2014; Denli and Huang, 2008; Guitton et al., 2007; Yoon and Marfurt, 2006; Youn and Zhou, 2001). Here, we address the second type of artifact; the first type is beyond the scope of this paper, since it requires non-conventional data acquisition or additional assumptions.

Considering the issue of polarity reversal and backscattering artifacts, and the fact that several images for different wave modes are difficult to interpret, we seek an imaging condition that outputs an attribute of the Earth's reflectivity into a single image. This single image should facilitate interpretation and provide a concise description of the imaged structures. In addition, we intend to assign a clear physical explanation to images obtained with this imaging condition.

We propose a new imaging condition that captures all wave modes into a single image, with attenuated backscattering artifacts and without polarity reversal at normal incidence. Our imaging condition is derived from the energy conservation principle of an elastic wavefield.

3.2 Theory

We use energy conservation laws analogous to the acoustic case (Rocha et al., 2015) to derive a function that measures the energy of a wavefield. This energy function also enables us to form an imaging condition for two extrapolated elastic wavefields from source and receivers.

3.2.1 Wavefield extrapolation

For an isotropic medium enclosed by a domain $\Omega \subset \mathbb{R}^3$, we can write a wave equation for the displacement vector with no external sources (Aki and Richards, 2002):

$$\rho\ddot{\mathbf{U}} = \nabla\left[\lambda\left(\nabla\cdot\mathbf{U}\right)\right] + \nabla\left[\mu\cdot\left(\nabla\mathbf{U} + \nabla\mathbf{U}^{\mathrm{T}}\right)\right] \tag{3.1}$$

In equation 3.1, the elastic wavefield is a function of space ($\mathbf{x}$), time (t) and experiment index (e): $\mathbf{U}\left(e,\mathbf{x},t\right)$ for $\mathbf{x}\in\Omega$ and $t\in[0,T]$. Since elastic waves propagate at finite speed, we can take the spatial domain Ω large enough, and then assume homogeneous boundary conditions for $\mathbf{U}$ and its derivatives, which means $\mathbf{U}$ and its derivatives vanish on the boundary of Ω ($\partial\Omega$) for all $t\in[0,T]$. The density and the Lamé parameters are functions of space: $\rho\left(\mathbf{x}\right)$, $\lambda\left(\mathbf{x}\right)$, and $\mu\left(\mathbf{x}\right)$, and we assume these parameters vary slowly in Ω, which allows us to neglect their spatial derivatives, thus leading to a different wave equation:

$$\rho\ddot{\mathbf{U}} = \lambda\left[\nabla\left(\nabla\cdot\mathbf{U}\right)\right] + \mu\left[\nabla\cdot\left(\nabla\mathbf{U} + \nabla\mathbf{U}^{\mathrm{T}}\right)\right] \tag{3.2}$$

Equation 3.2 can be used to extrapolate elastic wavefield for arbitrary sources, assuming that we know the spatial distribution of parameters ρ,λ and μ.

3.2.2 Elastic wavefield energy

The total energy of an acoustic wavefield is conserved, i.e., we can write (Appendix 3.6.1)

$$\dot{E}(t) = \int_{\Omega}\dot{U}(\ddot{U} - c^2\nabla^2 U)d\mathbf{x} = 0\ . \tag{3.3}$$

In expression 3.3, superscript dot indicates time diferentiation. We develop the energy conservation expression for elastic wavefields analogously, by multiplying the time derivative

of the displacement wavefield (i.e. particle velocity) with the corresponding wave equation, followed by integration over the whole physical domain Ω. If we apply the dot product between the wave equation in equation 3.2 and $\dot{\mathbf{U}}$, we obtain

$$\rho\dot{\mathbf{U}}\cdot\ddot{\mathbf{U}} = \lambda\left[\dot{\mathbf{U}}\cdot\left[\nabla\left(\nabla\cdot\mathbf{U}\right)\right]\right] + \mu\left[\dot{\mathbf{U}}\cdot\left[\nabla\cdot\left(\nabla\mathbf{U}+\nabla\mathbf{U}^{\mathrm{T}}\right)\right]\right] \ . \tag{3.4}$$

Rearranging the term on the left-hand side by the chain rule leads to

$$\frac{1}{2}\frac{\partial}{\partial t}\rho|\dot{\mathbf{U}}|^2 = \lambda\left[\dot{\mathbf{U}}\cdot\left[\nabla\left(\nabla\cdot\mathbf{U}\right)\right]\right] + \mu\left[\dot{\mathbf{U}}\cdot\left[\nabla\cdot\left(\nabla\mathbf{U}+\nabla\mathbf{U}^{\mathrm{T}}\right)\right]\right] \ , \tag{3.5}$$

and integrating over the whole domain, we obtain

$$\frac{1}{2}\frac{\partial}{\partial t}\int_{\Omega}\rho|\dot{\mathbf{U}}|^2\ d\mathbf{x} = \int_{\Omega}\lambda\left[\dot{\mathbf{U}}\cdot\left[\nabla\left(\nabla\cdot\mathbf{U}\right)\right]\right]d\mathbf{x} + \int_{\Omega}\mu\left[\dot{\mathbf{U}}\cdot\left[\nabla\cdot\left(\nabla\mathbf{U}+\nabla\mathbf{U}^{\mathrm{T}}\right)\right]\right]\ d\mathbf{x}\ . \tag{3.6}$$

We can develop the two terms on the right-hand side of equation 3.6 separately. For the first term, using integration by parts, we obtain

$$\int_{\Omega}\lambda\left[\dot{\mathbf{U}}\cdot\left[\nabla\left(\nabla\cdot\mathbf{U}\right)\right]\right]d\mathbf{x} = \int_{\Omega}\lambda\left[\nabla\cdot\left[\dot{\mathbf{U}}\left(\nabla\cdot\mathbf{U}\right)\right]\right]\ d\mathbf{x} - \int_{\Omega}\lambda\left(\nabla\cdot\dot{\mathbf{U}}\right)\left(\nabla\cdot\mathbf{U}\right)d\mathbf{x}\ . \tag{3.7}$$

The first term on the right-hand side of equation 3.7 can be turned into a surface integral by the Divergence Theorem (Boas, 2006), thus becoming zero; both the wavefield $\mathbf{U}$ and its derivatives vanish on the boundary $\partial\Omega$, as explained in the preceding section:

$$\int_{\Omega}\lambda\left[\nabla\cdot\left[\dot{\mathbf{U}}\left(\nabla\cdot\mathbf{U}\right)\right]\right]d\mathbf{x} = \int_{\partial\Omega}\lambda\left[\dot{\mathbf{U}}\left(\nabla\cdot\mathbf{U}\right)\right]\cdot\mathbf{n}\ d\mathbf{x} = 0\ . \tag{3.8}$$

Therefore, equation 3.7 becomes

$$\int_{\Omega}\lambda\left[\dot{\mathbf{U}}\cdot\left[\nabla\left(\nabla\cdot\mathbf{U}\right)\right]\right]d\mathbf{x} = -\int_{\Omega}\lambda\left(\nabla\cdot\dot{\mathbf{U}}\right)\left(\nabla\cdot\mathbf{U}\right)d\mathbf{x}\ . \tag{3.9}$$

Using the chain rule, we arrange the term on the right-hand side as follows:

$$\int_{\Omega}\lambda\left(\nabla\cdot\dot{\mathbf{U}}\right)\left(\nabla\cdot\mathbf{U}\right)d\mathbf{x} = \frac{1}{2}\frac{\partial}{\partial t}\int_{\Omega}\lambda|\nabla\cdot\mathbf{U}|^2\ d\mathbf{x}\ . \tag{3.10}$$

Similarly, for the second term on the right-hand side of equation 3.6, we use integration by parts:

$$\int_{\Omega} \mu \left[\dot{\mathbf{U}} \cdot \left[\nabla \cdot \left(\nabla \mathbf{U} + \nabla \mathbf{U}^{\mathrm{T}}\right)\right]\right] d\mathbf{x} = \int_{\Omega} \mu \left[\nabla \cdot \left[\dot{\mathbf{U}} \cdot \left(\nabla \mathbf{U} + \nabla \mathbf{U}^{\mathrm{T}}\right)\right]\right] d\mathbf{x} - \int_{\Omega} \mu \left(\nabla \dot{\mathbf{U}}\right) : \left(\nabla \mathbf{U} + \nabla \mathbf{U}^{\mathrm{T}}\right) d\mathbf{x} \tag{3.11}$$

where the symbol : indicates the Frobenius product between two matrices (Appendix 3.6.2). First integral of the right-hand side goes to zero by divergence theorem; therefore, we can write

$$\int_{\Omega} \mu \left[\dot{\mathbf{U}} \cdot \left[\nabla \cdot \left(\nabla \mathbf{U} + \nabla \mathbf{U}^{\mathrm{T}}\right)\right]\right] d\mathbf{x} = -\int_{\Omega} \mu \left(\nabla \dot{\mathbf{U}}\right) : \left(\nabla \mathbf{U} + \nabla \mathbf{U}^{\mathrm{T}}\right) d\mathbf{x} \tag{3.12}$$

Developing further, using the properties of the Frobenius product, we obtain:

$$\begin{aligned} -\int_{\Omega} \mu \left(\nabla \cdot \dot{\mathbf{U}}\right) : \left(\nabla \mathbf{U} + \nabla \mathbf{U}^{\mathrm{T}}\right) d\mathbf{x} &= -\int_{\Omega} \mu \mathrm{Tr} \left[\nabla \dot{\mathbf{U}} \left(\nabla \mathbf{U}^{\mathrm{T}} + \nabla \mathbf{U}\right)\right] d\mathbf{x} \\ &= -\int_{\Omega} \mu \mathrm{Tr} \left[\nabla \dot{\mathbf{U}} \nabla \mathbf{U}^{\mathrm{T}} + \nabla \dot{\mathbf{U}} \nabla \mathbf{U}\right] d\mathbf{x} \\ &= -\frac{1}{2} \frac{\partial}{\partial t} \int_{\Omega} \mu \mathrm{Tr} \left[\nabla \mathbf{U} \nabla \mathbf{U}^{\mathrm{T}} + \nabla \mathbf{U} \nabla \mathbf{U}\right] d\mathbf{x} \\ &= -\frac{1}{2} \frac{\partial}{\partial t} \int_{\Omega} \mu \left[\nabla \mathbf{U} : \nabla \mathbf{U} + \nabla \mathbf{U} : \nabla \mathbf{U}^{\mathrm{T}}\right] d\mathbf{x}. \end{aligned} \tag{3.13}$$

Rewriting equation 3.6 with the new right-hand side terms from equations 3.10 and 3.13 leads to

$$\frac{1}{2} \frac{\partial}{\partial t} \int_{\Omega} \rho \|\dot{\mathbf{U}}\|^2 + \lambda \|\nabla \cdot \mathbf{U}\|^2 + \mu \left[\nabla \mathbf{U} : \nabla \mathbf{U} + \nabla \mathbf{U} : \nabla \mathbf{U}^{\mathrm{T}}\right] \, d\mathbf{x} = 0 \,, \tag{3.14}$$

and we obtain an expression in the form $\dot{E}(t) = 0$, which is the mathematical formulation of the conservation of energy over time. Therefore, the function

$$E(t) = \frac{1}{2} \int_{\Omega} \rho \|\dot{\mathbf{U}}\|^2 + \lambda \|\nabla \cdot \mathbf{U}\|^2 + \mu \left[\nabla \mathbf{U} : \nabla \mathbf{U} + \nabla \mathbf{U} : \nabla \mathbf{U}^{\mathrm{T}}\right] \, d\mathbf{x} \tag{3.15}$$

measures the total energy of the wavefield within a domain.

3.2.3 Physical Interpretation

Equation 3.15 can be treated as a special case of the total energy of a wavefield in an anisotropic medium:

$$E(t) = \frac{1}{2} \int_{\Omega} \rho \|\dot{\mathbf{U}}\|^2 + \underline{\underline{\mathbf{c}}}\ \mathbf{e} : \mathbf{e}\ d\mathbf{x}\ . \tag{3.16}$$

where $\underline{\underline{\mathbf{c}}}$ is the 4th-rank stiffness tensor and $\mathbf{e} = \frac{1}{2}\left(\nabla\mathbf{U} + \nabla\mathbf{U}^{\mathrm{T}}\right)$ is the strain tensor. The first term in the integrand of equation 3.16 represents the kinetic energy of the wavefield, and the second term is the strain energy, which represents the potential energy of the wavefield. Substituting the stiffness coefficients for the isotropic case in equation 3.16, we obtain equation 3.15 (Appendix 3.6.3). Therefore, the second and third terms in equation 3.15 are equal to the strain energy function for isotropic media. Due to the fact that the wavefield vanishes at $\partial\Omega$, the total energy in equation 3.15 can be simplified further, considering that the second-order spatial derivatives of the wavefield are continuous (Appendix 3.6.4):

$$E(t) = \frac{1}{2} \int_{\Omega} \rho \|\dot{\mathbf{U}}\|^2 + (\lambda + \mu)\, \|\nabla \cdot \mathbf{U}\|^2 + \mu \nabla\mathbf{U} : \nabla\mathbf{U}\ d\mathbf{x}\ . \tag{3.17}$$

It is important to note that the total energy derivation depends on the wave equation used in the first place. Equation 3.17 could also be derived starting from the following wave equation

$$\rho\ddot{\mathbf{U}} = (\lambda + \mu)\, \nabla\left(\nabla \cdot \mathbf{U}\right) + \mu\nabla^2\mathbf{U}\ . \tag{3.18}$$

which is equivalent to equation 3.2 if the second-order spatial derivatives of the wavefield are continuous (Appendix 3.6.5).

3.2.4 Imaging condition

Considering two wavefields $\mathbf{U}$ and $\mathbf{V}$, and the elastic energy norm in equation 3.17, we define the following inner product:

$$< \mathbf{U}, \mathbf{V} >_E = \int_0^T \int_{\Omega} \rho\dot{\mathbf{U}} \cdot \dot{\mathbf{V}} + (\lambda + \mu)\left(\nabla \cdot \mathbf{U}\right)\left(\nabla \cdot \mathbf{V}\right) + \mu\nabla\mathbf{U} : \nabla\mathbf{V}\ d\mathbf{x}\ . \tag{3.19}$$

We propose a new elastic imaging condition based on the inner product in equation 3.19 between source and receiver wavefields, followed by integration over time and experiments:

$$I_E = \sum_{e,t} \left[\rho \dot{\mathbf{U}} \cdot \dot{\mathbf{V}} + (\lambda + \mu) (\nabla \cdot \mathbf{U})(\nabla \cdot \mathbf{V}) + \mu \, (\nabla \mathbf{U}) : (\nabla \mathbf{V}) \right] . \tag{3.20}$$

Here, $\mathbf{U}(e, \mathbf{x}, t)$ and $\mathbf{V}(e, \mathbf{x}, t)$ are the source and receiver vector wavefields, respectively, and $I_E(\mathbf{x})$ is a scalar image obtained based on the elastic wavefields. We can describe this imaging condition as a dot product between the following multidimensional vectors:

$$\Box \mathbf{U} = \left\{ \sqrt{\rho} \dot{\mathbf{U}}, \sqrt{\lambda + \mu} (\nabla \cdot \mathbf{U}), \sqrt{\mu} (\nabla \mathbf{U}) \right\}, \tag{3.21}$$

$$\Box \mathbf{V} = \left\{ \sqrt{\rho} \dot{\mathbf{V}}, \sqrt{\lambda + \mu} (\nabla \cdot \mathbf{V}), \sqrt{\mu} (\nabla \mathbf{V}) \right\} . \tag{3.22}$$

Equations 3.21 and 3.36 define multidimensional vectors with thirteen components, of which three components are the wavefield time derivatives, $\dot{\mathbf{U}}$ and $\dot{\mathbf{V}}$, one is the scaled divergence of the wavefields, $\nabla \cdot \mathbf{U}$ and $\nabla \cdot \mathbf{V}$, and nine are from the tensor wavefield gradient, $\nabla \mathbf{U}$ and $\nabla \mathbf{V}$.

Therefore, we can rewrite equation 3.20 as

$$I_E = \sum_{e,t} \Box \mathbf{U} \cdot \Box \mathbf{V} . \tag{3.23}$$

This expression is analogous to the similar imaging condition developed for acoustic wavefields (Rocha et al., 2015), and has similar physical interpretation and application, as discussed in the next section.

3.2.5 Backscattering attenuation

Vectors $\Box \mathbf{U}$ and $\Box \mathbf{V}$ are related to the polarization and propagation direction of the elastic wavefields $\mathbf{U}$ and $\mathbf{V}$. Decomposing the wavefield $\mathbf{U}$ in plane waves, we obtain

$$\mathbf{U} = \mathbf{u}_0 e^{i\omega(\mathbf{p} \cdot \mathbf{x} - t)} , \tag{3.24}$$

where $\mathbf{u}_0$ is the polarization vector, $\mathbf{p}$ is the slowness vector, and ω is the frequency. We assume that ω is large and that the vectors $\mathbf{u}_0$ and $\mathbf{p}$ are slowly varying in space and

time, which makes the spatial and temporal derivatives of $\mathbf{u}_0$ and $\mathbf{p}$ small compared to ω. Substituting the plane wave definition in equation 3.24 as trial solution of the elastic equation in 3.18, we obtain an expression that is equivalent to the Christoffel equation when reduced to isotropic media (Appendix 3.6.6):

$$\rho\mathbf{u}_0 = (\lambda+\mu)\,(\mathbf{u}_0\cdot\mathbf{p})\,\mathbf{p} + \mu\,(\mathbf{p}\cdot\mathbf{p})\,\mathbf{u}_0\ . \tag{3.25}$$

Multiplying equation 3.25 by $\mathbf{u}_0$ leads to

$$\rho|\mathbf{u}_0|^2 = (\lambda+\mu)\,(\mathbf{u}_0\cdot\mathbf{p})^2 + \mu|\mathbf{p}|^2|\mathbf{u}_0|^2\ . \tag{3.26}$$

The terms in equation 3.26 are present in the definition of $\Box\mathbf{U}$, stated in equation 3.21:

$$\begin{aligned}
\dot{\mathbf{U}} &= -i\omega\mathbf{u}_0 e^{i\omega(\mathbf{p}\cdot\mathbf{x}-t)}\ , &(3.27)\\
\nabla\cdot\mathbf{U} &= i\omega\,(\mathbf{u}_0\cdot\mathbf{p})\,e^{i\omega(\mathbf{p}\cdot\mathbf{x}-t)}\ , &(3.28)\\
\nabla\mathbf{U} &= i\omega\,(\mathbf{u}_0\otimes\mathbf{p})\,e^{i\omega(\mathbf{p}\cdot\mathbf{x}-t)}\ , &(3.29)
\end{aligned}$$

where the symbol $\otimes$ indicates the outer product between two vectors, resulting in a matrix. Therefore, the dot product of $\Box\mathbf{U}$ with itself is

$$\begin{aligned}
\Box\mathbf{U}\cdot\Box\mathbf{U} &= \rho\dot{\mathbf{U}}\cdot\dot{\mathbf{U}} + (\lambda+\mu)\,(\nabla\cdot\mathbf{U})(\nabla\cdot\mathbf{U}) + \mu\ (\nabla\mathbf{U}):(\nabla\mathbf{U})\\
&= -\omega^2\Big[\rho|\mathbf{u}_0|^2 + (\lambda+\mu)\,(\mathbf{u}_0\cdot\mathbf{p})^2 + \mu|\mathbf{p}|^2|\mathbf{u}_0|^2\Big]e^{2i\omega(\mathbf{p}\cdot\mathbf{x}-t)}\ . \qquad (3.30)
\end{aligned}$$

We seek to define an imaging condition that attenuates waves of the source and receiver wavefields propagating along the same path and with the same polarization, i.e., elastic backscattering. Defining $(\Box\mathbf{V})^\dagger$ as

$$(\Box\mathbf{V})^\dagger = \Big\{-\sqrt{\rho}\mathbf{V}_t, \sqrt{\lambda+\mu}(\nabla\cdot\mathbf{V}), \sqrt{\mu}(\nabla\mathbf{V})\Big\}\ , \tag{3.31}$$

we can compute the dot product between $\Box\mathbf{U}$ and $(\Box\mathbf{V})^\dagger$ as

$$\begin{aligned}
\Box\mathbf{U}\cdot(\Box\mathbf{V})^\dagger &= -\rho\dot{\mathbf{U}}\cdot\dot{\mathbf{V}} + (\lambda+\mu)\,(\nabla\cdot\mathbf{U})(\nabla\cdot\mathbf{V}) + \mu\ (\nabla\mathbf{U}):(\nabla\mathbf{V})\\
&= \omega^2\Big[\rho|\mathbf{u}_0|^2 - (\lambda+\mu)\,(\mathbf{u}_0\cdot\mathbf{p})^2 - \mu|\mathbf{p}|^2|\mathbf{u}_0|^2\Big]e^{2i\omega(\mathbf{p}\cdot\mathbf{x}-t)}\ . \qquad (3.32)
\end{aligned}$$

Using the relation in equation 3.26, we obtain

$$\Box\mathbf{U}\cdot(\Box\mathbf{V})^{\dagger}=0\ , \tag{3.33}$$

i.e., the dot product is zero everywhere except at locations where reflectors exist or different wave modes interact, since the vectors $\mathbf{p}$ and $\mathbf{u}_0$ are different for $\mathbf{U}$ and $\mathbf{V}$ at these locations. Therefore, the dot product in equation 3.33 suppresses the events that propagate on the same path and have the same polarization. Such events include reflection backscattering, diving, direct and head waves from the same wave modes. Therefore, the imaging condition

$$I_E^{\dagger}=\sum_{e,t}\Box\mathbf{U}\cdot(\Box\mathbf{V})^{\dagger} \tag{3.34}$$

attenuates backscattering artifacts in elastic RTM images.

Due to the multidimensional character of $\Box\mathbf{U}$ and $(\Box\mathbf{V})^{\dagger}$, which have thirteen components, it is difficult to visualize the orthogonality of these vectors in the imaging condition shown in equation 3.34 for the most general case possible. However, we can illustrate this idea by simple schematic examples.

Figures 3.1 and 3.2 show schematic plots describing imaging experiments using plane waves with S- and P- pure polarizations. Figures 3.1(a) and 3.2(a) describe the evolution of the source wavefields for S- and P- wave modes, with vertical plane wave sources located at $x=0$ km. Extrapolating the data backwards in time from the vertical receiver at $x=5$ km generates receiver wavefields for S- and P- wave modes shown in Figures 3.1(b) and 3.2(b), respectively. In Figures 3.1 and 3.2, the thick arrows represent the directions of polarization, and the thin arrows represent the slowness vectors. The vectors $\Box\mathbf{U}$ and $(\Box\mathbf{V})^{\dagger}$ for the S-wave experiment in Figure 3.1 are obtained using the definitions in equations 3.21 and 3.31, $\mathbf{u}_0=\{0,0,1\}$ and $\mathbf{p}=\left\{\sqrt{\frac{\rho}{\mu}},0,0\right\}$:

$$\Box\mathbf{U} = i\omega\sqrt{\rho}\,\{-1,0,1\}\,e^{i\omega(\mathbf{p}\cdot\mathbf{x}-t)}, \tag{3.35}$$

$$(\Box\mathbf{V})^{\dagger} = i\omega\sqrt{\rho}\,\{1,0,1\}\,e^{i\omega(\mathbf{p}\cdot\mathbf{x}-t)}, \tag{3.36}$$

which leads to

$$\square\mathbf{U} \cdot (\square\mathbf{V})^{\dagger} = 0. \tag{3.37}$$

The vectors $\square\mathbf{U}$ and $(\square\mathbf{V})^{\dagger}$ for the P-wave experiment in Figure 3.2 are also obtained using equations 3.21 and 3.31, $\mathbf{u}_0 = \{1, 0, 0\}$ and $\mathbf{p} = \left\{\sqrt{\frac{\rho}{\lambda+2\mu}}, 0, 0\right\}$:

$$\square\mathbf{U} = i\omega\sqrt{\rho}\left\{-1, \sqrt{\frac{\lambda+\mu}{\lambda+2\mu}}, \sqrt{\frac{\mu}{\lambda+2\mu}}\right\} e^{i\omega(\mathbf{p}\cdot\mathbf{x}-t)}, \tag{3.38}$$

$$(\square\mathbf{V})^{\dagger} = i\omega\sqrt{\rho}\left\{1, \sqrt{\frac{\lambda+\mu}{\lambda+2\mu}}, \sqrt{\frac{\mu}{\lambda+2\mu}}\right\} e^{i\omega(\mathbf{p}\cdot\mathbf{x}-t)}\ , \tag{3.39}$$

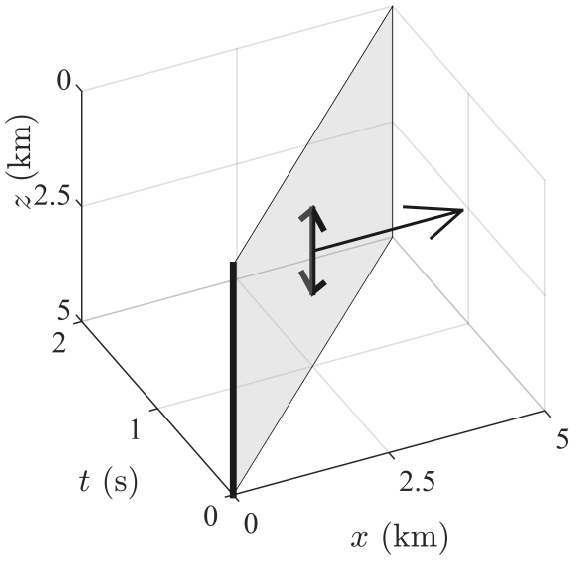
which also leads to

$$\square\mathbf{U} \cdot (\square\mathbf{V})^{\dagger} = 0. \tag{3.40}$$

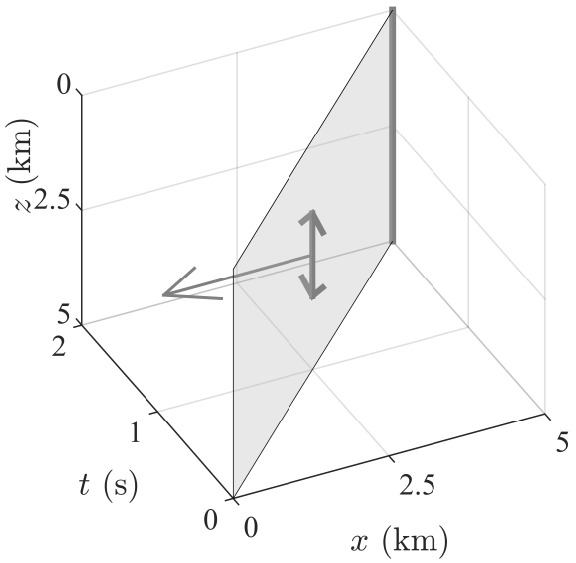
3.3 Examples

Using a simple model with a horizontal reflector at $z = 1.5$ km and a vertical displacement source function, we test the proposed imaging condition and compare it with the conventional imaging conditions (Figures 3.3, 3.4, and 3.5). The presence of the reflector in the migration velocity leads to a velocity contrast, causing backscattering artifacts in these numerical experiments. These artifacts appear most prominently in the images using displacement components (Figure 3.3), PP (Figure 3.4(a)) and SS (Figure 3.4(d)) images. In the PS (Figure 3.4(b)) and SP (Figure 3.4(c)) images, the converted reflections do not correlate with the incident waves, thus freeing these images from backscattering artifacts. Note the polarity reversal at normal incidence in Figures 3.3(b), 3.3(c), 3.4(b), and 3.4(c). The energy imaging condition also shows backscattering artifacts (Figure 3.5(c)). However, the modified energy imaging condition from equation 3.34 effectively attenuates the backscattering artifacts (Figure 3.5(d)).

Figures 3.6-3.7 show a simple 3D elastic experiment, with constant medium parameters and a horizontal reflector. We use a vertical oriented displacement source to generate the

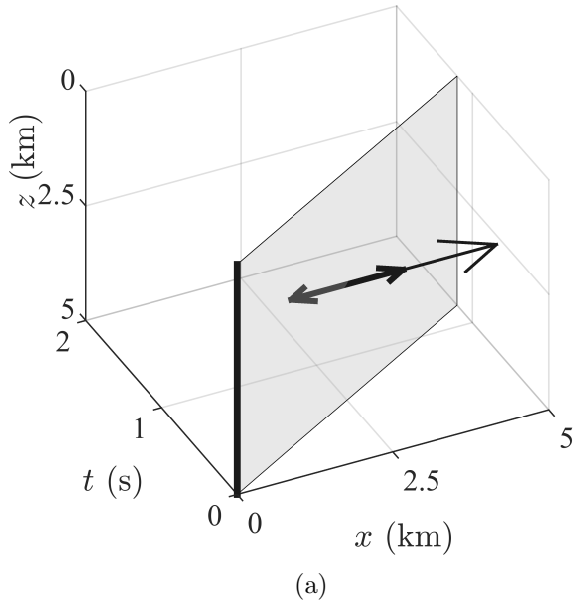


(a)

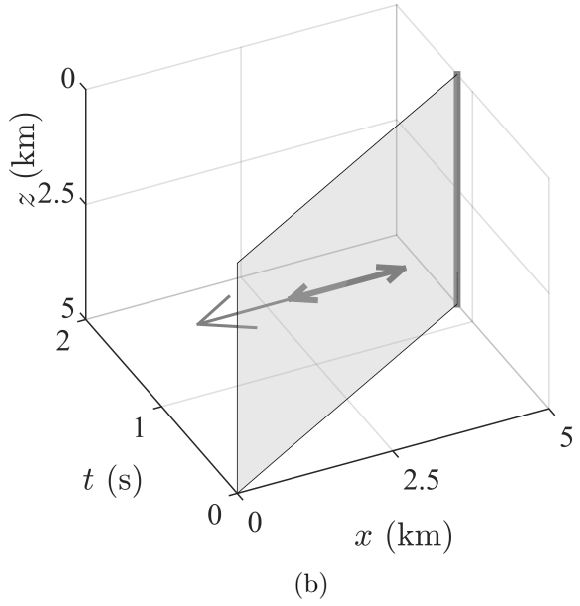


(b)

Figure 3.1: Schematic plots showing the evolution of elastic plane-wave wavefields over time, originated by (a) a vertical source at $x = 0$ km and (b) a vertical receiver line at $x = 5$ km. Notice that (b) represents a wavefield propagating backwards in time. The thick arrows represent pure S-wave polarization, and the thin arrows represent the slowness vectors.



(a)



(b)

Figure 3.2: Schematic plots showing the evolution of elastic plane-wave wavefields over time, originated by (a) a vertical source at $x = 0$ km and (b) a vertical receiver line at $x = 5$ km. Notice that (b) represents a wavefield propagating backwards in time. The thick arrows represent pure P-wave polarization, and the thin arrows represent the slowness vectors. Note that the wavefields propagate faster than the ones in Figure 3.1 since P-wave velocity is faster than S-wave velocity.

source wavefield, and we record the receiver data everywhere at the surface. Similarly to the 2D experiment in Figures 3.3-3.5, images in Figure 3.6 present fake mode artifacts (caused by the fact that we do not record the entire elastic wavefield at the surface), polarity reversal at normal incidence when correlating different wave modes, and backscattering artifacts when correlating same wave modes (the reflector is present at the migration velocity). Figure 3.7(a) shows a PP image, and Figures 3.7(b)-3.7(d) show the application of the energy imaging condition: a total energy image (Figure 3.7(b)) shows no polarity reversal at normal incidence, but still shows backscattering artifacts; however, the application of the imaging condition in equation 3.34 forms the image in Figure 3.7(c), with attenuated backscattering artifacts compared to Figure 3.7(b). Although the fake mode artifacts are present in Figure 3.7(c), stacking over a considerable number of shots attenuates this type of artifacts, as seen in Figure 3.7(d).

Figure 3.8 shows stacked images using the Marmousi (Bourgeois et al., 1991) model in order to test our new elastic imaging condition in a more realistic model. The migration velocity is a smoothed version of the stratigraphic velocity, which is used to generate synthetic data. Using the conventional imaging conditions for PP and PS wave modes, we obtain the images in Figure 3.8(a) and 3.8(c), respectively. Artifacts due to direct/diving waves and some residual backscattering created by the heterogeneities from the model are present in both conventional images. In addition, a Laplacian filter is applied on the PP image (Figure 3.8(b)); however, the application of a Laplacian operator on elastic images is an ad hoc filtering procedure that is not supported by elastic wavefield theory. Figure 3.8(c) also shows the effects of a non-constructive stack due to polarity reversal artifacts at normal incidence. We attenuate all these artifacts in Figure 3.8(d) using the imaging condition from equation 3.34. Similarly to the 3D experiment in Figures 3.7(c) and 3.7(d), using our new imaging condition, the individual elastic images for shots have only fake mode artifacts, which are attenuated after stacking, leading to a good quality image, as seen in Figure 3.8(d).

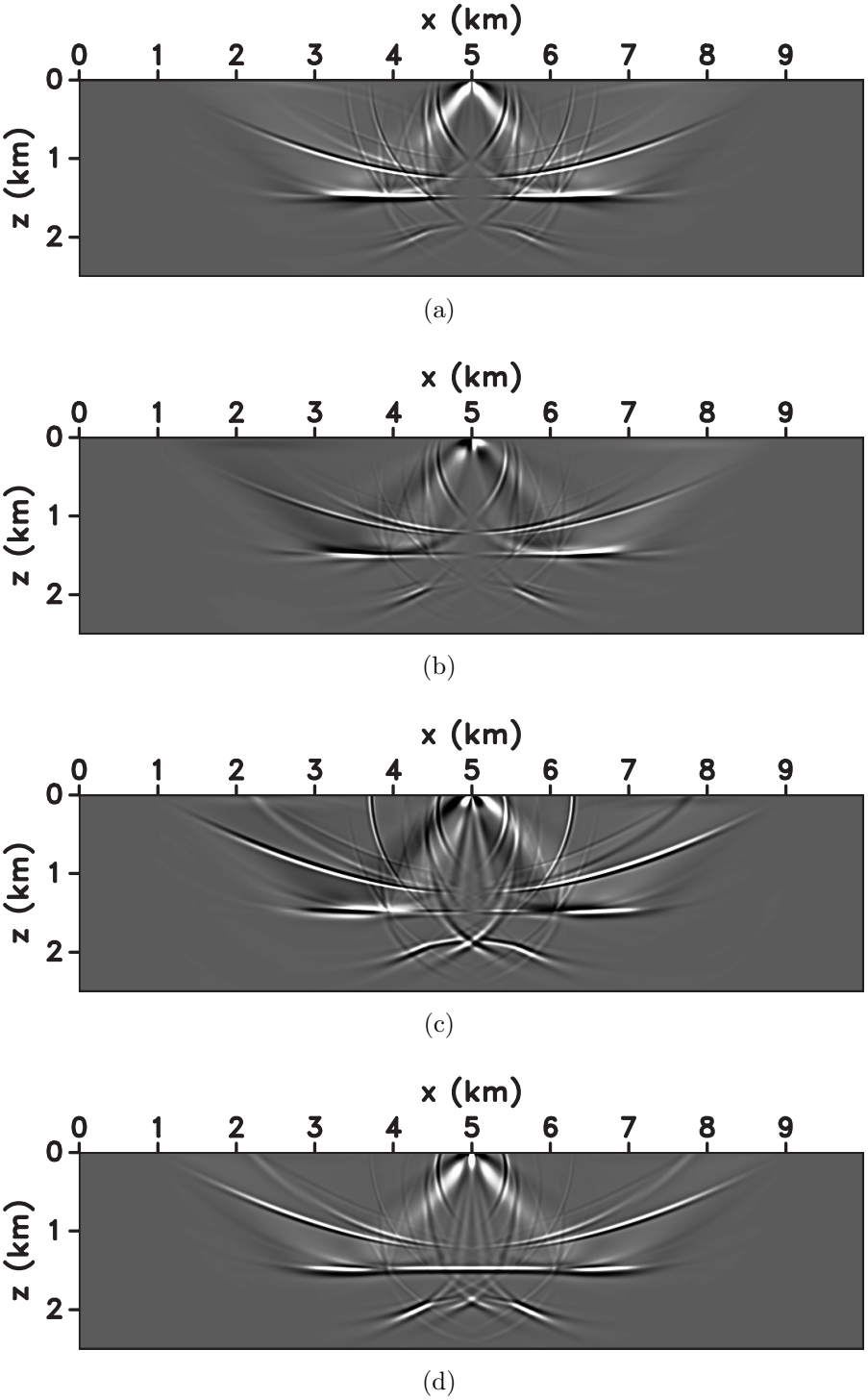


Figure 3.3: Imaging conditions using displacement components for a horizontal reflector with a vertical displacement source at $x = 5$ km: (a) U_xV_x, (b) U_xV_z, (c) U_zV_x, and (d) U_zV_z image, where $\{U_x, U_z\}$ and $\{V_x, V_z\}$ are the horizontal and vertical components of the source and receiver wavefields, respectively. The type of artifacts that are present in all images occur due to the fake modes, which are generated when injecting an incomplete displacement field in the receiver wavefield. Polarity reversal at normal incidence occurs for (b) and (c). The reflector is present in the migration velocity to generate backscattering artifacts, which are visible in all images.

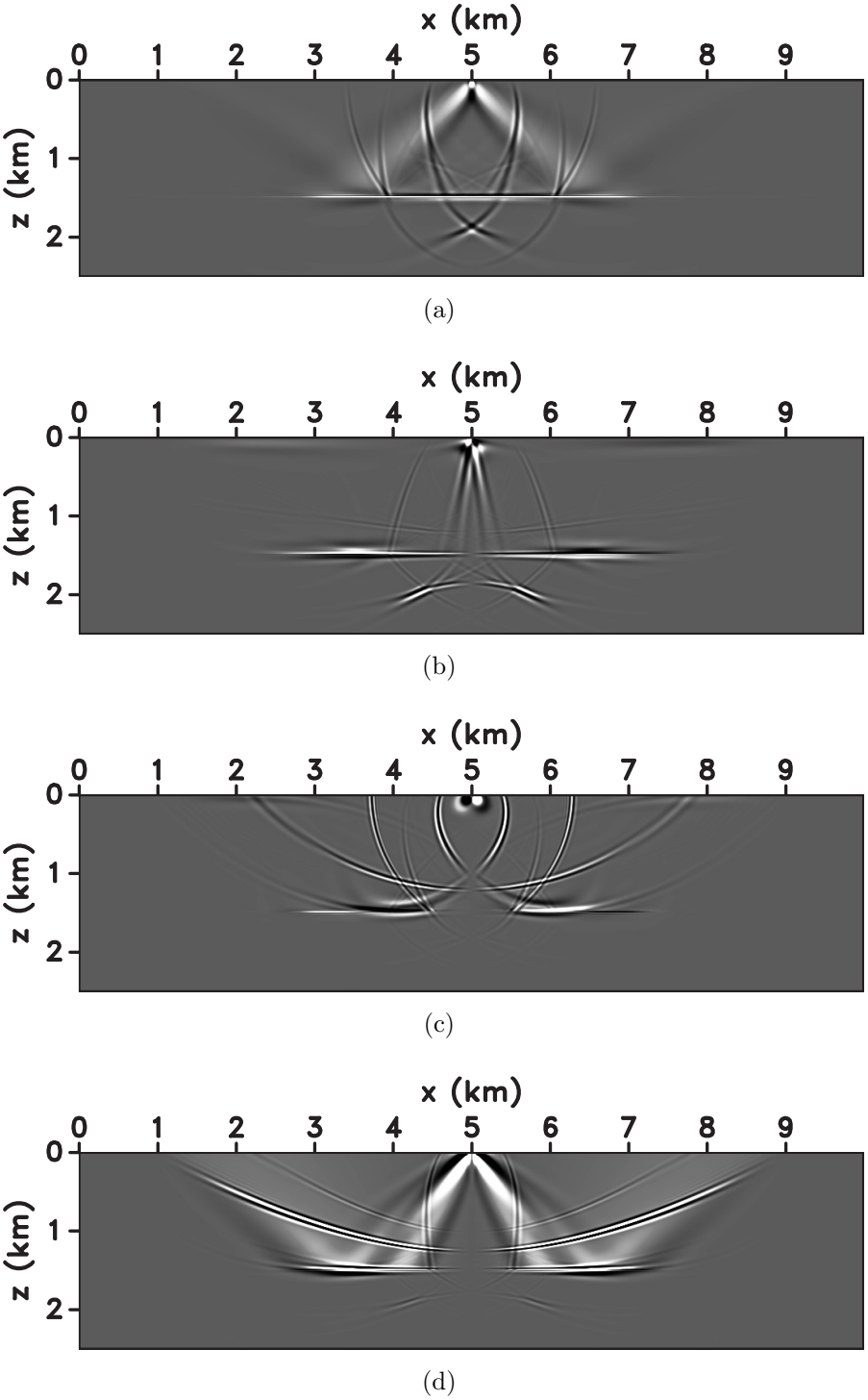


Figure 3.4: Imaging conditions using potentials for a horizontal reflector with a vertical displacement source at $x = 5$ km: (a) PP, (b) PS, (c) SP, and (d) SS image. Fake modes artifacts are also present in these images, analogously to Figure 3.3. The presence of a velocity contrast and the correlation between same wave modes in (a) and (d) generates backscattering artifacts, and the correlation between different wave modes in (b) and (c) generates polarity reversal at normal incidence.

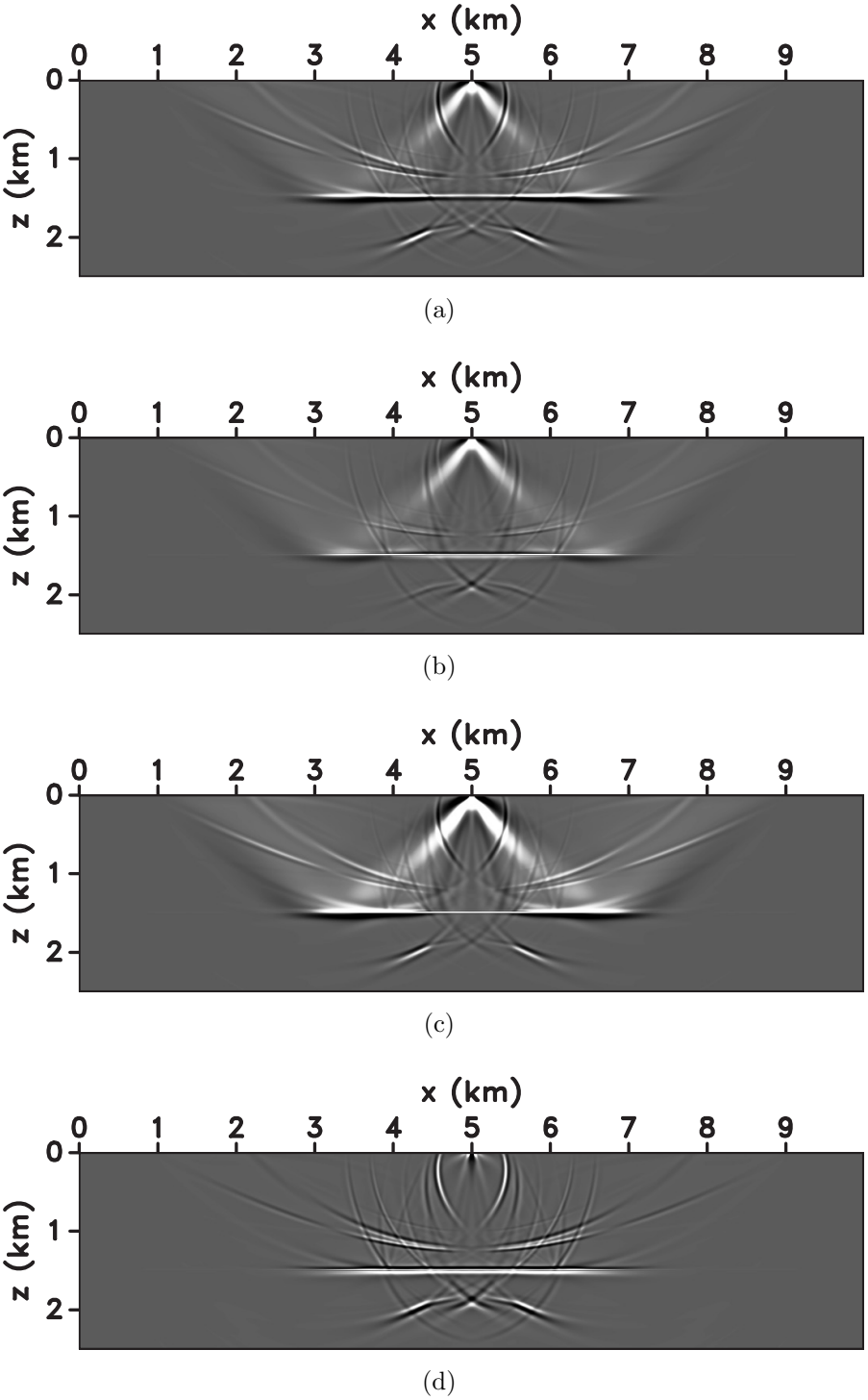


Figure 3.5: Individual terms of the energy imaging condition for a horizontal reflector present in the migration velocity, and a vertical displacement source at $x = 5$ km: (a) kinetic energy, (b) strain energy, (c) total energy and (d) imaging condition in equation 3.34. Comparing with other images from Figures 3.3-3.5, (d) is the only image with attenuated backscattering artifacts and without polarity reversal at normal incidence.

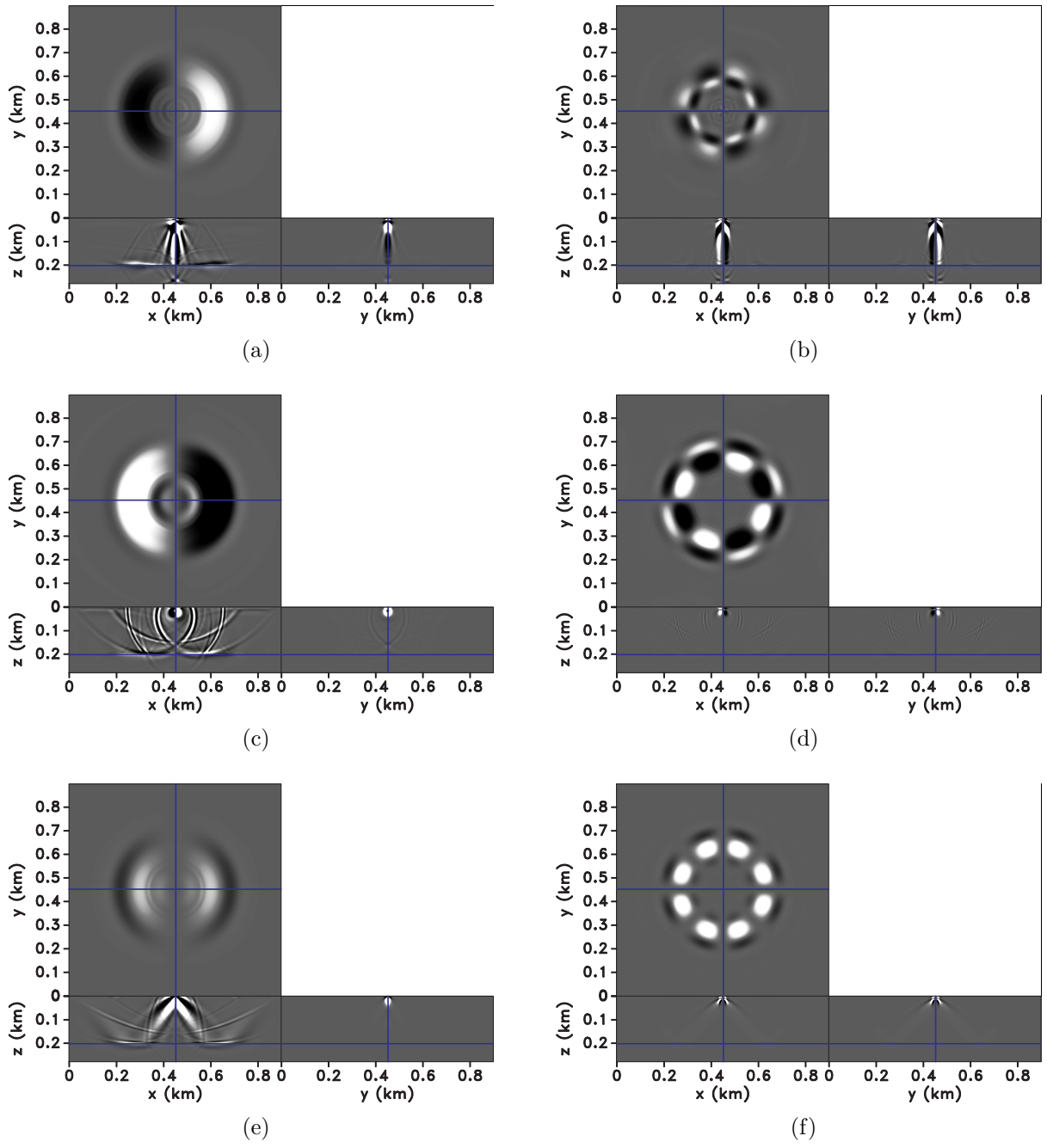


Figure 3.6: Images using conventional imaging conditions for a 3D elastic experiment with a horizontal reflector located at $z = 0.2$ km: (a) PS_y, (b) PS_z, (c) S_yP (d) S_zP, (e) S_yS_y, and (f) S_zS_z images. For images using correlation between the same wave modes, backscattering artifacts exist in (e) and (f); for the other images, which use correlation between different wave modes, polarity reversal occurs at normal incidence.

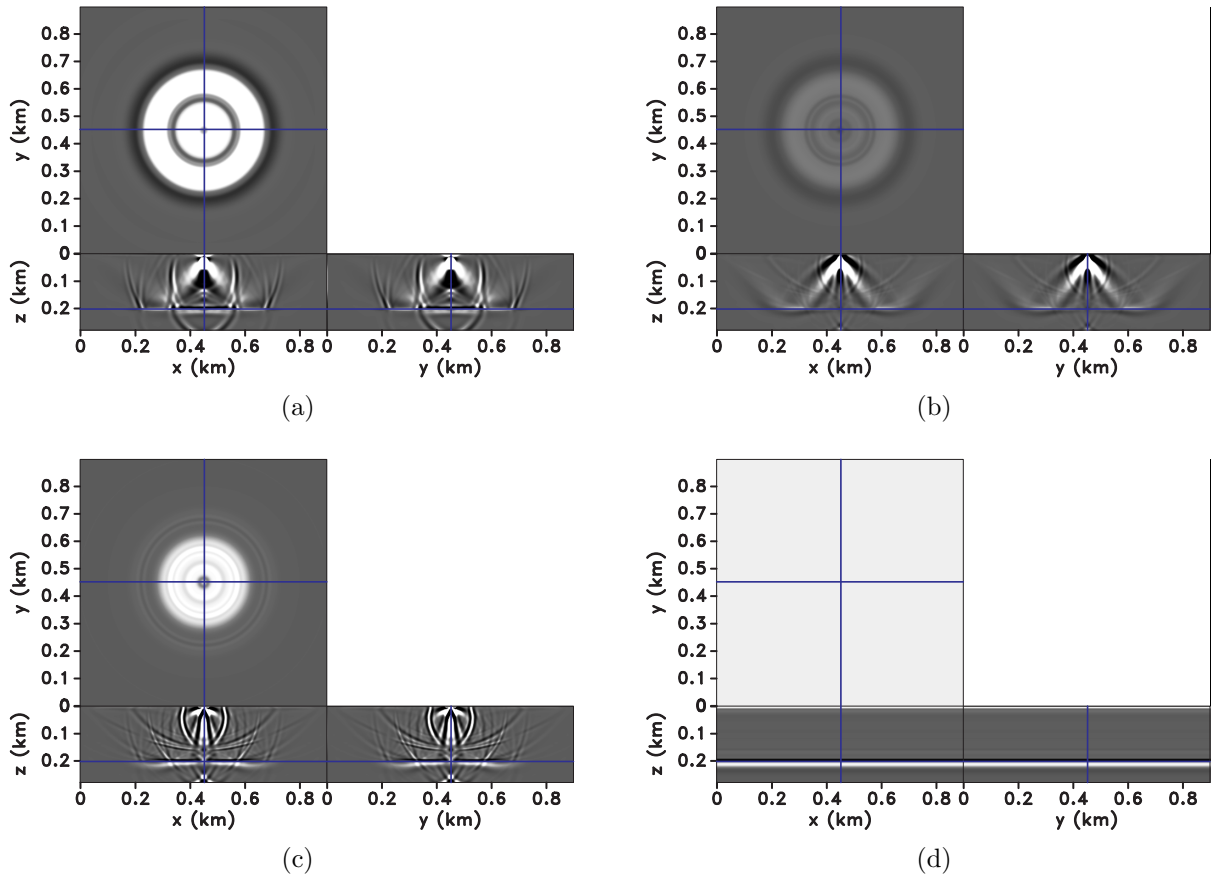
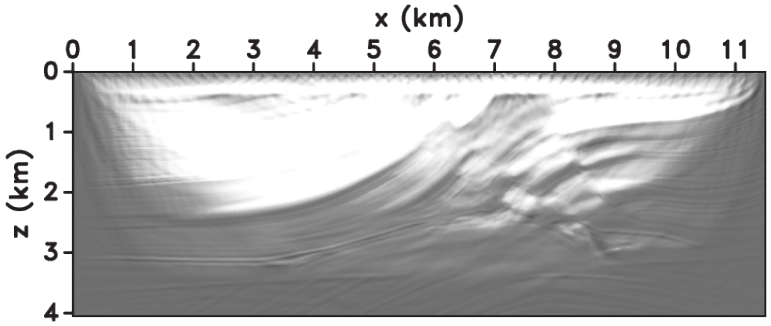
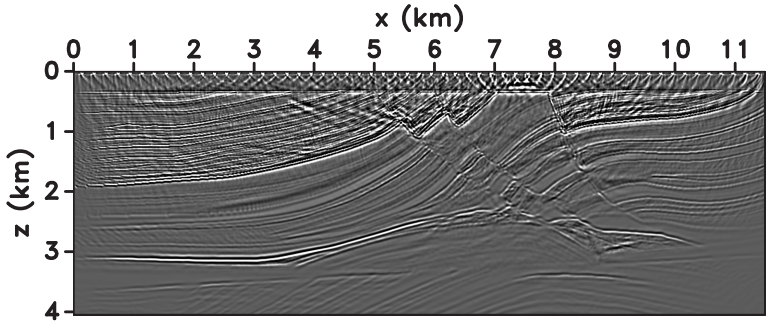


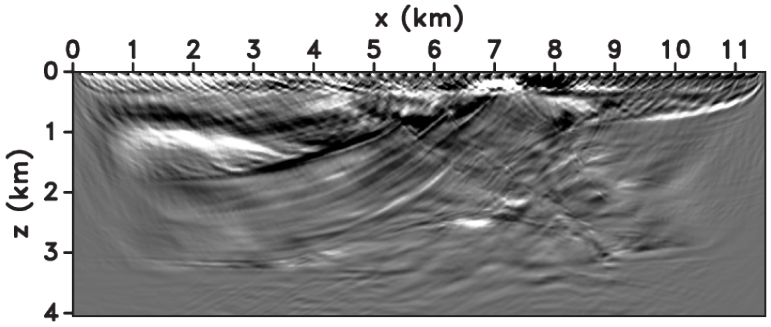
Figure 3.7: (a) PP image and images using energy imaging conditions for a 3D elastic experiment with a horizontal reflector located at $z = 0.2$ km, (b) total energy imaging condition, and (c) imaging condition from equation 3.34. Although (c) still has fake mode artifacts, stacking over shots attenuates this artifacts, as seen in (d), which is a stacked version of (c) using shots at every point at the surface.



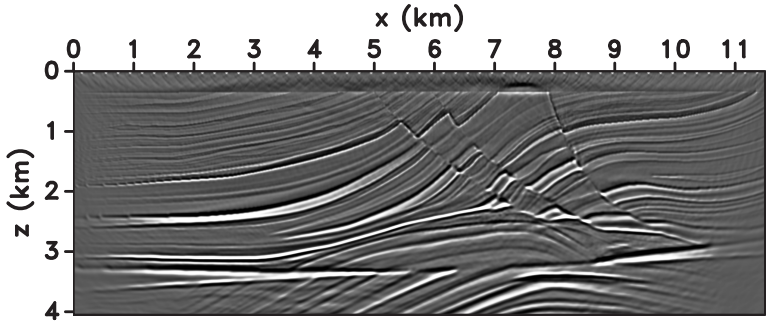
(a)



(b)



(c)



(d)

Figure 3.8: Experiment on Marmousi model. (a) PP image, (b) Laplacian filter applied on the PP image in (a), (c) PS image, and (d) energy imaging condition in equation 3.34. The image in (d) shows no artifacts from polarity reversal and attenuated backscattering energy compared to the conventional images in (a) and (c), and higher quality compared to (b).

3.4 Conclusions

The energy imaging condition offers an alternative to the conventional imaging conditions, which use potentials or displacement components. This alternative combines all wave modes into a single image and does not suffer from polarity reversal, as is the case for conventional images using converted modes, either with potentials or displacements. The energy imaging condition accounts for wavefield directionality, including the wavefield propagation and polarization directions. We describe this imaging condition as the projection between the multidimensional vectors $\Box\mathbf{U}$ and $\Box\mathbf{V}$ (built using the extrapolated wavefields $\mathbf{U}$ and $\mathbf{V}$), whose terms contain information about wavefield directionality. By exploiting this directionality, we are able to attenuate the backscattering artifacts in the imaging, in a way that is similar to the case with acoustic waves.

3.5 Acknowledgments

We would like to thank sponsor companies of the Consortium Project on Seismic Inverse Methods for Complex Structures, whose support made this research possible. We acknowledge Yuting Duan, who provided the elastic modeling code for this research. The reproducible numeric examples in this paper use the Madagascar open-source software package (Fomel et al., 2013) freely available from http://www.ahay.org.

3.6 Appendices

The appendices below elucidate specific points of this current chapter.

3.6.1 Conservation of energy for an acoustic wavefield

Given a solution to the acoustic wave equation:

$$\ddot{U} - c^2\nabla^2 U = 0 \ , \tag{3.41}$$

we can define the energy at a time t (Evans, 1997; McOwen, 2003) as

$$E(t) = \frac{1}{2}\int_{\mathbb{R}^N} (\dot{U}^2 + c^2|\nabla U|^2) d\mathbf{x} \ . \tag{3.42}$$

The energy gives a integral measure of the regularity of U for first-order derivation.

Let us define the domain in which the solution is valid by $\Omega \in \mathbb{R}^N$. Considering c is a finite propagation speed, one can assume U and its derivatives are close to zero on the boundary $\partial\Omega$ for all times if Ω is sufficiently large. The conservation of energy means $\dot{E}(t) = 0$, therefore, deriving $E(t)$ within the domain Ω yields

$$\dot{E}(t) = \int_{\Omega} (\dot{U}\ddot{U} + c^2 \nabla U \cdot \nabla \dot{U}) d\mathbf{x} \, . \tag{3.43}$$

The second term in the integrand can be integrated by parts:

$$\int_{\Omega} c^2 (\nabla U \cdot \nabla \dot{U}) dx = \int_{\Omega} c^2 \nabla \cdot (\dot{U} \nabla U) dx - \int_{\Omega} c^2 (\dot{U} \nabla^2 U) d\mathbf{x} \, . \tag{3.44}$$

The first term of the right-hand side can be turned into a surface integral by Divergence Theorem and then it goes to zero, since the U and its derivatives vanish on the boundary $\partial\Omega$. Substituting the remaining term in equation 3.43 yields

$$\dot{E}(t) = \int_{\Omega} \dot{U} (\ddot{U} - c^2 \nabla^2 U) d\mathbf{x} = 0 \, , \tag{3.45}$$

because the wavefield u satisfies the wave-equation in equation 3.41.

The energy norm for an acoustic wavefield can be considered as a special case of the isotropic energy norm. Using vector calculus identities, equation 3.18 can be rewritten as

$$\rho \ddot{\mathbf{U}} = (\lambda + 2\mu) \left[\nabla \left(\nabla \cdot \mathbf{U} \right) \right] - \mu \left[\nabla \times \left(\nabla \times \mathbf{U} \right) \right] . \tag{3.46}$$

If the particle displacement $\mathbf{U}$ is has only compressional behavior, the term $[\nabla \times (\nabla \times \mathbf{U})]$ is zero. Equation 3.46 becomes

$$\rho \ddot{\mathbf{U}} = (\lambda + 2\mu) \left[\nabla \left(\nabla \cdot \mathbf{U} \right) \right] \tag{3.47}$$

The energy norm for this wave equation is

$$E(t) = \frac{1}{2} \int_{\Omega} \rho \|\dot{\mathbf{U}}\|^2 + (\lambda + 2\mu) \|\nabla \cdot \mathbf{U}\|^2 d\mathbf{x} \tag{3.48}$$

In this form, the energy norm refers to the particle displacement $\mathbf{U}$. In a more general sense, this norm applies for any wavefield. We know that the particle velocity $\mathbf{S}$ is only 90 degrees

out of phase from $\mathbf{U}$. Therefore:

$$E(t) = \frac{1}{2}\int_{\Omega} \rho\|\dot{\mathbf{S}}\|^2 + (\lambda + 2\mu)\,\|\nabla \cdot \mathbf{S}\|^2 d\mathbf{x} \tag{3.49}$$

This can also be explained by deriving equation 3.48 in time, obtaining equation 3.49. The equations that relate particle velocity and pressure from continuum mechanics are (Webster, 2000)

$$\rho\dot{\mathbf{S}} = -\nabla p \tag{3.50}$$

$$\nabla \cdot \mathbf{S} = -\frac{1}{(\lambda + 2\mu)}\dot{p} \tag{3.51}$$

Rewriting the two equations above in terms of the norms:

$$\rho^2\|\dot{\mathbf{S}}\|^2 = -\|\nabla p\|^2 \tag{3.52}$$

$$\|\nabla \cdot \mathbf{S}\|^2 = -\frac{1}{(\lambda + 2\mu)^2}\|\dot{p}\|^2 \tag{3.53}$$

Substituting these last expressions in equation 3.49, we obtain

$$E(t) = -\frac{1}{2}\int_{\Omega} \frac{\|\nabla p\|^2}{\rho} + \frac{1}{(\lambda + 2\mu)}\|\dot{p}\|^2 d\mathbf{x} \tag{3.54}$$

Scaling this energy measure by $\rho\,(\lambda + 2\mu)$:

$$E(t) = -\frac{1}{2}\int_{\Omega} \rho\|\dot{p}\|^2 + (\lambda + 2\mu)\,\|\nabla p\|^2 d\mathbf{x} \tag{3.55}$$

which is equivalent to equation 3.42, considering U as the scalar pressure field, and $c = \sqrt{\frac{\lambda+2\mu}{\rho}}$.

3.6.2 Frobenius product and norm

The Frobenius norm is the most common matrix norm in numerical linear algebra. Consider an arbitrary matrix $A_{M\times N}$, this norm is defined as (Golub and Loan, 1996)

$$||A||_F = \sqrt{\sum_{i=1}^{M}\sum_{j=1}^{N} |a_{ij}|^2}\ . \tag{3.56}$$

We can also define the norm based on the inner product of associate matrices. Given matrices A and B, we can define the Frobenius product:

$$< A, B >_F = A : B = \sum_{i=1}^{M} \sum_{j=1}^{N} a_{ij} b_{ij} \ , \tag{3.57}$$

where A and B are of dimension $M \times N$. This product can also be written in matrix form as

$$< A, B >_F = A : B = \mathrm{Tr}(A^{\mathrm{T}} B) = \mathrm{Tr}(A B^{\mathrm{T}}) \ . \tag{3.58}$$

Then, we can write the Frobenius norm:

$$||A||_F = \sqrt{\mathrm{Tr}(A A^{\mathrm{T}})} \ , \tag{3.59}$$

3.6.3 Strain-energy function in isotropic media

In a general elastic medium subject to infinitesimal strains, the strain-energy function is (Slawinski, 2003)

$$E(\epsilon) = \frac{1}{2} c_{ijlk} \epsilon_{kl} \epsilon_{ij}. \tag{3.60}$$

where c_{ijlk} is an element of the stiffness tensor $\mathbf{c}$ and ϵ_{ij} is an element of the strain tensor $\mathbf{e}$. The repeated indices i, j, k, l imply summation, following the Einstein convention. For an isotropic medium, the stiffness coefficients are (Aki and Richards, 2002)

$$c_{ijlk} = \lambda \delta_{ij} \delta_{kl} + \mu \delta_{ik} \delta_{jl} + \mu \delta_{il} \delta_{jk}, \tag{3.61}$$

where δ_{ij} is the Kronecker delta function, λ and μ are the Lamé parameters. Substituting equation 3.61 in equation 3.60, we obtain

$$E(\epsilon) = \frac{1}{2} \left[\lambda \delta_{ij} \delta_{kl} + \mu \delta_{ik} \delta_{jl} + \mu \delta_{il} \delta_{jk} \right] \epsilon_{kl} \epsilon_{ij}. \tag{3.62}$$

Considering the Kronecker delta function is equal to unity for equal indices and zero otherwise, we develop each term and obtain

$$E(\epsilon) = \frac{1}{2}\left[\lambda\epsilon_{ii}\epsilon_{kk} + \mu\epsilon_{ij}\epsilon_{ij} + \mu\epsilon_{ji}\epsilon_{ij}\right]. \tag{3.63}$$

These implicit summations can be written in matrix form as

$$E(\mathbf{e}) = \frac{1}{2}\left[\lambda \mathrm{Tr}[\mathbf{e}]\mathrm{Tr}[\mathbf{e}] + \mu\left(\mathbf{e} : \mathbf{e}\right) + \mu\left(\mathbf{e} : \mathbf{e}^{\mathrm{T}}\right)\right]. \tag{3.64}$$

As the strain tensor is symmetric, we obtain

$$E(\mathbf{e}) = \frac{1}{2}\left[\lambda\left(\mathrm{Tr}[\mathbf{e}]\right)^2 + 2\mu\left(\mathbf{e} : \mathbf{e}\right)\right]. \tag{3.65}$$

The strain tensor $\mathbf{e}$ is function of the wavefield derivatives

$$\mathbf{e} = \frac{1}{2}\left[\nabla\mathbf{U} + \nabla\mathbf{U}^{\mathrm{T}}\right] \tag{3.66}$$

Substituting, we have

$$\begin{aligned} E(\mathbf{e}) &= \frac{1}{2}\left[\lambda\|\nabla\cdot\mathbf{U}\|^2 + 2\mu\left(\frac{1}{2}\left(\nabla\mathbf{U} + \nabla\mathbf{U}^{\mathrm{T}}\right) : \frac{1}{2}\left(\nabla\mathbf{U} + \nabla\mathbf{U}^{\mathrm{T}}\right)\right)\right] \\ &= \frac{1}{2}\left[\lambda\|\nabla\cdot\mathbf{U}\|^2 + \frac{1}{2}\mu\left(\nabla\mathbf{U} : \nabla\mathbf{U} + 2\nabla\mathbf{U} : \nabla\mathbf{U}^{\mathrm{T}} + \nabla\mathbf{U}^{\mathrm{T}} : \nabla\mathbf{U}^{\mathrm{T}}\right)\right] \\ &= \frac{1}{2}\left[\lambda\|\nabla\cdot\mathbf{U}\|^2 + \mu\left(\nabla\mathbf{U} : \nabla\mathbf{U} + \nabla\mathbf{U} : \nabla\mathbf{U}^{\mathrm{T}}\right)\right] \end{aligned} \tag{3.67}$$

which corresponds to the potential energy terms of equation 3.15.

3.6.4 Terms not accountable for the total energy

Integrating the strain energy function for the isotropic case (equation 3.67) over the whole spatial domain:

$$E_{\mathbf{e}} = \frac{1}{2}\int_{\Omega} \lambda\|\nabla\cdot\mathbf{U}\|^2 + \mu\left(\nabla\mathbf{U} : \nabla\mathbf{U} + \nabla\mathbf{U} : \nabla\mathbf{U}^{\mathrm{T}}\right)\, d\mathbf{x} \tag{3.68}$$

where the gradient of the displacement vector consists of the following elements

$$\nabla\mathbf{U} = \frac{\partial U_i}{\partial x_j} = \begin{bmatrix} U_{1,1} & U_{1,2} & U_{1,3} \\ U_{2,1} & U_{2,2} & U_{2,3} \\ U_{3,1} & U_{3,2} & U_{3,3} \end{bmatrix} \tag{3.69}$$

Rewriting equation 3.68 in terms of these elements:

$$\begin{aligned} E_{\mathbf{e}} &= \frac{1}{2}\int_{\Omega} \lambda\|\nabla\cdot\mathbf{U}\|^2 + \mu\left(\nabla\mathbf{U}:\nabla\mathbf{U} + U_{i,i}^2 + 2U_{2,1}U_{1,2} + 2U_{2,3}U_{3,2} + 2U_{1,3}U_{3,1}\right)\ d\mathbf{x} \\ &= \frac{1}{2}\int_{\Omega} \lambda\|\nabla\cdot\mathbf{U}\|^2 + \mu\left(\nabla\mathbf{U}:\nabla\mathbf{U}\right) + \mu\left(U_{i,i}\right)^2 + \mu\left(U_{i,j}U_{j,i} - U_{i,i}U_{j,j}\right)\ d\mathbf{x} \\ &= \frac{1}{2}\int_{\Omega} \left(\lambda+\mu\right)\|\nabla\cdot\mathbf{U}\|^2 + \mu\left(\nabla\mathbf{U}:\nabla\mathbf{U}\right) + \mu\left(U_{i,j}U_{j,i} - U_{i,i}U_{j,j}\right)\ d\mathbf{x}. \end{aligned} \tag{3.70}$$

The terms $(U_{i,j}U_{j,i} - U_{i,i}U_{j,j})$ integrated over the whole spatial domain become zero. We can show it by an example with x and y, with $\mathbf{U} = \{u, v, w\}$:

$$\int\int \left(\frac{\partial u}{\partial y}\frac{\partial v}{\partial x} - \frac{\partial u}{\partial x}\frac{\partial v}{\partial y}\right) dxdy \tag{3.71}$$

Integrating by parts the second term of the integrand, and assuming u and v vanish at the boundaries, we have

$$\int\int \left(\frac{\partial u}{\partial y}\frac{\partial v}{\partial x} + u\frac{\partial^2 v}{\partial x\partial y}\right) dxdy \tag{3.72}$$

Integrating the second term by parts once more, and assuming u and v have second-order continuous derivatives, we have

$$\int\int \left(\frac{\partial u}{\partial y}\frac{\partial v}{\partial x} - \frac{\partial u}{\partial y}\frac{\partial v}{\partial x}\right) dxdy = 0 \tag{3.73}$$

which makes the total energy in equations 3.15 and 3.17 equivalent when second-order derivatives are continuous.

3.6.5 Elastic wave equation and continuity of second-order derivatives

Equation 3.2 has the following wave equation

$$\rho\ddot{\mathbf{U}} = \lambda\left[\nabla\left(\nabla\cdot\mathbf{U}\right)\right] + \mu\left[\nabla\cdot\left(\nabla\mathbf{U} + \nabla\mathbf{U}^{\mathrm{T}}\right)\right] \tag{3.74}$$

which can be simplified further if using the following calculus identity

$$\left[\nabla\cdot\left(\nabla\mathbf{U} + \nabla\mathbf{U}^{\mathrm{T}}\right)\right] = \nabla\left(\nabla\cdot\mathbf{U}\right) + \nabla^2\mathbf{U} \tag{3.75}$$

In index form, this identity is

$$U_{j,ij} + U_{i,jj} = U_{j,ji} + U_{i,jj} \tag{3.76}$$

Notice that, for this identity to be valid, second-order derivatives must be continuous, so we can interchange derivatives for $U_{j,ij} = U_{j,ji}$. Therefore, assuming this identity to be true, equation 3.74 becomes

$$\rho\ddot{\mathbf{U}} = (\lambda + \mu)\,\nabla\,(\nabla \cdot \mathbf{U}) + \mu\nabla^2\mathbf{U}\ . \tag{3.77}$$

3.6.6 Christoffel equation for isotropic media

The Christoffel equation for anisotropic media is (Musgrave, 1970; Tsvankin, 2012)

$$\left[c_{ijkl}p_j p_l - \rho\delta_{ik}\right] u_k = 0\ , \tag{3.78}$$

where δ_{ij} is the Kronecker delta function, c_{ijkl} is the stiffness tensor, $\rho\,(\mathbf{x})$ is the density, u_k is the k-th component of the polarization vector $\mathbf{u}_0$, and p_j and p_l are the j-th and l-th components of the slowness vector $\mathbf{p}$. We can rewrite equation (3.78) as

$$\rho u_i = u_k c_{ijkl} p_j p_l\ . \tag{3.79}$$

The stiffness coefficients for isotropic media are defined by

$$c_{ijlk} = \lambda\delta_{ij}\delta_{kl} + \mu\delta_{ik}\delta_{jl} + \mu\delta_{il}\delta_{jk}\ , \tag{3.80}$$

where $\lambda\,(\mathbf{x})$ and $\mu\,(\mathbf{x})$ are the Lamé parameters. Substituting the isotropic stiffness definition in equation (3.79), we obtain

$$\begin{aligned}
\rho u_i &= u_k\left(\lambda\delta_{ij}\delta_{kl} + \mu\delta_{ik}\delta_{jl} + \mu\delta_{il}\delta_{jk}\right) p_j p_l\ , && (3.81)\\
&= u_k\left(\lambda p_i p_k + \mu\delta_{ik}p_j p_j + \mu p_i p_k\right)\ , && (3.82)\\
&= (\lambda + \mu)\left(u_k p_k\right) p_i + \mu\left(p_j p_j\right) u_i\ , && (3.83)
\end{aligned}$$

with summation over indices k and j. We can rewrite equation (3.83) in vector form as

$$\rho\mathbf{u}_0 = (\lambda + \mu)\left(\mathbf{u}_0 \cdot \mathbf{p}\right)\mathbf{p} + \mu(\mathbf{p} \cdot \mathbf{p})\mathbf{u}_0\ . \tag{3.84}$$

Finally, we can also rewrite the Christoffel equation in (3.84) in terms of P and S velocities:

$$\mathbf{u}_0 = \left(v_p^2 - v_s^2\right)(\mathbf{u}_0 \cdot \mathbf{p})\,\mathbf{p} + v_s^2(\mathbf{p} \cdot \mathbf{p})\mathbf{u}_0 \; . \tag{3.85}$$

CHAPTER 4

CONCLUSION

In this thesis, I introduce the concept of the energy norm of a wavefield and present its applications for two particular types of wavefields: acoustic (Chapter 2), and elastic (Chapter 3). Regardless of the degree of complexity of the wavefields, I find that the inner product derived from the energy norm serves as an elegant solution to persistent problems for both cases, since its definition and numerical implementation are simple (dot product between energy vectors) and require no additional information about the earth model, such as the reflector dip.

The simpler implementation proposed here compared to conventional methods is most important for the elastic case. Commonly, the displacement wavefields from both source and receiver sides contain both the compressional and transverse wave modes that need to be separated for some conventional imaging conditions. Wave-mode separation demands additional cost in the imaging process, and even more cost and complexity when the isotropic assumption is not satisfied. Alternatively, the energy imaging condition discussed in this thesis does not require wave-mode separation.

The main reason why the energy imaging condition delivers improved results compared to its conventional counterparts is the use of information about wavefield directionality, which is present in the energy vectors. Wavefield directionality is the key to distinguish artifacts from useful wave events, and by using the energy vectors, we are able to use this information implicitly in the imaging condition without significant additional cost. In contrast, other techniques used to obtain wavefield directionality information, such as Poynting vectors and extended image gathers, require explicit computation of reflection angles to suppress artifacts in the image.

Even though one does not need to explicitly compute reflection angles to suppress artifacts in the energy images, the reflection angle information is of great interest in the seismic industry, and can still be extracted from the obtained images. Therefore, developing this energy-norm angle decomposition is an important topic for future research.

Moreover, the energy norm can be defined for any type of wavefield for which we can formulate an energy measure that is conserved over time. An energy norm for anisotropic wavefields could extend the method discussed in this thesis. Similarly, imaging methods using electromagnetic wavefields, such as ground-penetrating radar, are subject to similar problems to those found in seismic imaging, and the energy norm can also be applied with similar effectiveness as for seismic wavefields.

REFERENCES CITED

Aki, K., and P. G. Richards, 2002, Quantitative seismology, 2 ed.: University Science Books.

Albertin, U., G. Shan, and J. Washbourne, 2013, Gradient orthogonalization in adjoint scattering-series inversion: Presented at the SEG Houston 2013 Annual Meeting.

Alkhalifah, T., 2015, Scattering-angle based filtering of the waveform inversion gradients: Geophysical Journal International, **200**, 363–373.

Almomin, A., and B. Biondi, 2012, Tomographic Full Waveform Inversion: Practical and Computationally Feasible Approach: Presented at the SEG Las Vegas 2012 Annual Meeting.

Balch, A. H., and C. Erdermir, 1994, Sign-change correction for prestack migration of P-S converted wave reflections: Geophysical Prospecting, **42**, 637–663.

Baysal, E., D. D. Kosloff, and J. W. C. Sherwood, 1983, Reverse time migration: Geophysics, **48**, 1514–1524.

Boas, M. L., 2006, Mathematical Methods in the Physical Sciences, 3 ed.: John Wiley & Sons.

Bourgeois, A., M. Bourget, P. Lailly, M. Poulet, P. Ricarte, and R. Versteeg, 1991, Marmousi, model and data: Presented at the 1990 EAGE workshop on Practical Aspects of Seismic Data Inversion.

Brandsberg-Dahl, S., N. Chemingui, D. Whitmore, S. Crawley, E. Klochikhina, and A. Valenciano, 2013, 3D RTM angle gathers using an inverse scattering imaging condition: Presented at the SEG Houston 2013 Annual Meeting.

Chang, W.-F., and G. A. McMechan, 1986, Reverse-time migration of offset vertical seismic profiling data using the excitation-time imaging condition: Geophysics, **51**, 67–84.

———, 1987, Elastic reverse-time migration: Geophysics, **52**, 1365–1375.

Chappel, J., A. Iqbal, and D. Abbot, 2010, A simplified approach to electromagnetism using geometric algebra. Available at http://arxiv.org/abs/1010.4947v2.

Chen, T., and L. Huang, 2014, Elastic reverse-time migration with an excitation amplitude imaging condition: Presented at the SEG Denver 2014 Annual Meeting.

Claerbout, J. F., 1971, Toward a unified theory of reflector mapping: Geophysics, **36**, 467–481.

———, 1985, Imaging the Earth's Interior: Blackwell Scientific Publications.

Cohen, J. K., and N. Bleistein, 1979, Velocity inversion procedure for acoustic waves: Geophysics, **44**, 1077–1087.

Costa, J. C., F. A. S. Neto, M. Alcantara, J. Schleicher, and A. Novais, 2009, Obliquity-correction imaging condition for reverse time migration: Geophysics, **74**, S57–S66.

Dellinger, J., and J. Etgen, 1990, Wave-field separation in two-dimensional anisotropic media: Geophysics, **55**, 914–919.

Denli, H., and L. Huang, 2008, Elastic-wave reverse-time migration with a wavefield-separation imaging condition: Presented at the SEG 2008 Annual Meeting.

Diaz, E., and P. Sava, 2015, Wavefield tomography using reverse time migration backscattering: Geophysics, **80**, R57–R69.

Douma, H., D. Yingst, I. Vasconcelos, and J. Tromp, 2010, On the connection between artifact filtering in reverse-time migration and adjoint tomography: Geophysics, **75**, S219–S223.

Duan, Y., and P. Sava, 2014a, Converted-waves imaging condition for elastic reverse-time migration: Presented at the SEG 2014 Denver Annual Meeting.

———, 2014b, Elastic reverse-time migration with OBS multiples: Presented at the SEG 2014 Denver Annual Meeting.

Etgen, J. T., 1988, Prestacked migration of P- and SV-waves: Presented at the SEG 1988 Annual Meeting.

Evans, L. C., 1997, Partial Differential Equations: American Mathematical Society, **19**.

Feynman, R. P., R. B. Leighton, and M. Sands, 1964, The feynman lectures on physics: Addison Wesley, **2**.

Fletcher, R. F., P. Fowler, P. Kitchenside, and U. Albertin, 2005, Suppresing artifacts in prestack reverse time migration: Presented at the SEG Houston 2005 Annual Meeting.

Fomel, S., P. Sava, I. Vlad, Y. Liu, and V. Bashkardin, 2013, Madagascar: open-source software project for multidimensional data analysis and reproducible computational experiments: Journal of Open Research Software, **1**.

Gao, F., P. Williamson, and H. Houllevigue, 2012, Full waveform inversion by deconvolution gradient method: Presented at the SEG Las Vegas 2012 Annual Meeting.

Gauthier, O., J. Virieux, and A. Tarantola, 1986, Two-dimensional nonlinear inversion of seismic waveforms:Numerical results: Geophysics, **51**, 1387–1403.

Golub, G. H., and C. F. V. Loan, 1996, Chapter 2 - Matrix Analysis, *in* Matrix computations, 3 ed.: John Hopkins University Press.

Guitton, A., B. Kaelin, and B. Biondi, 2007, Least-squares attenuation of reverse-time-migration artifacts: Geophysics, **72**, S19–S23.

Hindlet, F., and P. Kolb, 1988, Inversion of prestack field data: An application to 1-D acoustic media: Presented at the SEG Technical Program Expanded Abstracts.

Hokstad, K., R. Mittet, and M. Landrø, 1998, Elastic reverse time migration of marine walkaway vertical seismic profiling data: Geophysics, **63**, 1685–1695.

Jain, P. K., O. P. Ahuja, and K. Ahmed, 2004, Functional Analysis, 2 ed.: New age international.

Lailly, P., 1983, The seismic inverse problem as a sequence of before stack migrations: Conference on Inverse Scattering, Theory and Application: Presented at the Society of Industrial and Applied Mathematics, Expanded Abstracts, 206-220.

Levin, S. A., 1984, Principle of reverse-time migration: Geophysics, **49**, 581–583.

Liu, F., G. Zhang, S. A. Morton, and J. P. Leveille, 2011, An effective imaging condition for reverse-time migration using wavefield decomposition: Geophysics, **76**, S29–S39.

Margrave, G. F., and R. J. Ferguson, 1999, Wavefield extrapolation by nonstationary phase shift: Geophysics, **64**, 1067–1078.

McMechan, G. A., 1983, Migration by extrapolation of time dependent boundary values: Geophysical Prospecting, **31**, 413–420.

McOwen, R. C., 2003, Partial Differential Equations: Methods and Applications, 2 ed.: Prentice Hall.

Mora, P., 1989, Inversion = migration + tomography: Geophysics, **54**, 1575–1586.

Musgrave, M., 1970, Crystal Acoustics: Holden-Day.

Oristaglio, M. L., 1989, An inverse scattering formula that uses all the data: Inverse Problems, **5**, 1097–1105.

Perrone, F., and P. Sava, 2014, Wavefield tomography based on local image correlations: Geophysical Prospecting, **63**, 35–54.

Pestana, R., A. W. G. dos Santos, and E. S. Araujo, 2013, RTM imaging condition using impedance sensitivity kernel combined with Poynting vector: Presented at the 13th International Congress of The Brazilian Geophysical Society.

Plessix, R. E., 2006, A review of the adjoint-state method for computing the gradient of a functional with geophysical applications: Geophysical Journal International, **167**, 495–503.

Plessix, R. E., Y.-H. de Roech, and G. Chavent, 1999, Waveform inversion of reflection seismic data for kinematic parameters by local optimization: SIAM Journal on Scientific Computing, **20**, 1033–1052.

Plessix, R. E., P. Milcik, H. Rynja, A. Stopin, K. Matson, and S. Abri, 2013, Multiparameter full-waveform inversion: Marine and land examples: The Leading Edge, **32**, 1030–1038.

Rocha, D., N. Tanushev, and P. Sava, 2015, Acoustic wavefield imaging using the energy norm: Presented at the SEG New Orleans 2015 Annual Meeting.

Sava, P., 2014, A comparative review of wavefield tomography methods: Center for Wave Phenomena.

Sava, P., and S. Fomel, 2006, Time-shift imaging condition in seismic migration: Geophysics, **71**, S209–S217.

Sava, P., and I. Vasconcelos, 2011, Extended imaging condition for wave-equation migration: Geophysical Prospecting, **59**, 35–55.

Shan, G., Y. Wang, and U. Albertin, 2014, Wave Equation Migration Velocity Analysis by Wavefield Decomposition: Presented at the SEG Denver 2014 Annual Meeting.

Slawinski, M. A., 2003, Seismic waves and rays in elastic media, 1 ed.: Elsevier Science, **34**.

Suh, S. Y., and J. Cai, 2009, Reverse-time migration by fan filtering plus wavefield decomposition: Presented at the SEG Houston 2009 Annual Meeting.

Sun, S., and B. Wang, 2013, Improving salt boundary imaging using an RTM inverse sacttering imaging condition: Presented at the SEG Houston 2013 Annual Meeting.

Tang, Y., S. Lee, A. Baumstein, and D. Hinkley, 2013, Tomographically enhanced full wavefield inversion: Presented at the SEG Houston 2013 Annual Meeting.

Tanushev, N. M., B. Engquist, and R. Tsai, 2009, Gaussian beam decomposition of high frequency wave fields: Journal of Computational Physics, **228**, 8856–8871.

Tarantola, A., 1984, Inversion of seismic reflection data in the acoustic approximation: Geophysics, **49**, 1259–1266.

Tsvankin, I., 2012, Seismic signatures and analysis of reflection data in anisotropic media, 3 ed.: Society of Exploration Geophysicists.

Webster, J., 2000, Chapter 8.1 - The Wave Equation, *in* Mechanical variables measurement: solid, fluid and thermal, 1 ed.: CRC Press.

Whitmore, N. D., 1983, Iterative depth migration by backward time propagation: Presented at the SEG 1983 Annual Meeting.

Whitmore, N. D., and S. Crawley, 2012, Application of RTM inverse scattering imaging conditions: Presented at the SEG Las Vegas 2012 Annual Meeting.

Xu, S., F. Chen, B. Tang, and G. Lambare, 2014, Noise removal by migration of time-shift images: Geophysics, **79**, S105–S111.

Yan, J., and P. Sava, 2007, Elastic wavefield imaging with scalar and vector potentials: Presented at the SEG Denver 2007 Annual Meeting.

———, 2008, Isotropic angle-domain elastic reverse-time migration: Geophysics, **73**, S229–S239.

———, 2009, Elastic wave-mode separation for VTI media: Geophysics, **74**, WB19–WB32.

———, 2011, Improving the efficiency of elastic wave-mode separation for heterogeneous tti media: Geophysics, **76**, T65–T78.

Yan, R., and X.-B. Xie, 2010, The new angle-domain imaging condition for elastic RTM: Presented at the SEG Denver 2010 Annual Meeting.

———, 2012, An angle-domain imaging condition for elastic reverse time migration and its application to angle gather extraction: Geophysics, **77**, S105–S115.

Yang, T., and P. Sava, 2015, Image-domain wavefield tomography with extended common-image-point gathers: Geophysical Prospecting.

Yoon, K., and K. J. Marfurt, 2006, Reverse-time migration using the Poynting vector: Exploration Geophysics, **37**, 102–107.

Youn, O., and H. W. Zhou, 2001, Depth imaging with multiples: Geophysics, **66**, 246–255.

Zeidler, E., 1999, Applied Functional Analysis: Applications to Mathematical Physics: Springer, **108**.

Zhang, Y., and J. Sun, 2009, Practical issues in reverse time migration: true amplitude gathers, noise removal and harmonic source enconding: First Break, **27**, 53–59.

Zhe, J., and S. A. Greenhalg, 1997, Prestack multicomponent migration: Geophysics, **62**, 598–613.